Title: The spatial periodic computation of hippocampus-entorhinal circuit in navigation

Bo Zhang[1,2], and Jia Liu[2*]

[1] Beijing Academy of Artificial Intelligence, Beijing, 100084, China

[2] Tsinghua Laboratory of Brain and Intelligence & Department of Psychology, Tsinghua University, Beijing, 100084, China

*Correspondence shall be addressed to: JL, liujiathu@tsinghua.edu.cn

Abstract

To achieve the computational goal of navigating in both physical and mental spaces, the brain employs a cognitive map constructed by the global metrics of entorhinal grid cells and the local locations of hippocampal place cells. However, how these two regions work collaboratively in path integration remains little known. Here, we designed an object-matching task where human participants unknowingly manipulated object variants arranged in a ring-like structure around a central prototype. Functional MRI revealed a 3-fold spatial periodicity in hippocampal activity, which tracked path directions during navigation. Importantly, this spatial periodicity of the hippocampus was phase-locked with the well-documented 6-fold spatial periodicity of the entorhinal cortex, suggesting a periodic scaffold connecting these regions. Inspired by this empirical evidence, we proposed the E-H PhaseSync Model, an algorithm to formalize the interplay of spatial orientations encoded by grid cells and path directions encoded by place cells that leads to the emergence of 3-fold periodic vector fields in the hippocampus. The implementation of this model not only reproduced the hippocampal periodic activity but also, surprisingly, predicted a 3-fold periodicity embedded in behavior, which was confirmed by participants' behavioral performance. Taken together, this study suggests that the spatial periodicity originated from the population activity of entorhinal grid cells may serve as a scaffold in the hippocampal-entorhinal network, where hippocampal vector fields emerge as the neural basis for utilizing the cognitive map in navigation.

Introduction

The Cognitive map, introduced by Tolman (1948) and elaborated through the discovery of hippocampal place cells (O'Keefe and Dostrovsky, 1971), represents a mental framework of spatial and conceptual relationships (Epstein et al., 2017; Behrens et al., 2018; Bottini and Doeller, 2020) to facilitate knowledge retrieval and decision-making (Park et al., 2020; Toledo et al., 2020; Nyberg et al., 2022; De Cothi et al., 2022; Muhle-Karbe et al., 2023). However, how these abstract relationships by hippocampal place cells are actualized in navigating both spatial and conceptual spaces remain somewhat unclear. A recent study by Ormond and O'Keefe (2022) sheds light on this issue by unveiling the convergence sinks (ConSinks) of hippocampal place cells, which are vector fields encoding allocentric directions and distances. Specifically, these vector fields are distributed across environment and exhibit maximal activity when mice orient towards the goal. This finding underscores the role of hippocampal place cells in providing vector-based representations as navigational signals to reach the intended goal. In this study, we further asked how hippocampal vector fields, which represent the direction from self-location to the goal, are constructed during navigation.

Anatomically, the hippocampus (HPC) receives major projections from the upstream entorhinal cortex (ERC) (Witter and Amaral, 1991; van Groen et al., 2003; Garcia and Buffalo, 2020), and complete lesions of the ERC substantially disrupt place representations in precision and stability (Hales et al., 2014). Entorhinal grid cells, known for their hexagonal firing pattern as a metric for space (Hafting et al., 2005), are proposed by computational models as foundational for place field formation through phase vectors of multi-scale grid modules (Solstad et al., 2006; De Almeida et al., 2009; Bush et al., 2014; Bush et al., 2015; Bicanski and Burgess, 2019). Empirical evidence also demonstrates grid cells' role in tracking direction and velocity, essential for navigation (Sargolini et al., 2006; Munn et al., 2020; Gerlei et al., 2020; Morris and Derdikman, 2023). Those results collectively support the possibility that grid cells may serve as the geometric framework with periodic codes to promote the formation of hippocampal vector fields of place cells via the ERC-HPC circuitry. If this conjecture is valid, then we might expect to find spatial periodicity in the HPC, which would likely be a manifestation of hippocampal vector fields of place cells at the population level, based on the observation of the nearly invariant orientation and spacing of grid cells at populational level (Hafting et al., 2005; Stensola et al., 2015; Krupic et al., 2015; Gardner et al., 2022).

The examination of this idea requires simultaneously recording ERC and HPC activity at the populational level, putting great challenges on electrophysiological and two-photon calcium imaging on animals' brains. Functional MRI (fMRI), which offers a broader scope, have been employed to explore the spatial periodicity of entorhinal grid cells at the population level and successfully identify a 6-fold modulation when navigating in both spatial and conceptual spaces (Doeller et al., 2010; Constantinescu et al., 2016; Bao et al., 2019; Wagner et al., 2023; Raithel et al., 2023). Consequently, in this study we used fMRI with human participants to explore whether there is spatial periodicity in the HPC and, critically, whether this spatial periodicity, if observed, is phase-locked with that of the ERC.

To do this, we designed an object matching task, which required participants to morph the object variants to match the target prototype by navigating in a 2-dimensional object space (Fig. 1). To explore potential spatial periodicity in the HPC, the starting-locations were arranged in a ring-shaped pattern, with each location corresponding to a unique conceptual direction towards the goal ranging from 0º to 360º. Spectral analysis revealed a spatial periodicity of 3-fold modulation in the CA1 region of the HPC, whose phase was closely coupled with the spatial periodicity of 6-fold modulation in the ERC. Based on this empirical finding, we developed the "E-H PhaseSync" model to elucidate the formation of hippocampal vector fields from the projection of grid cell population. Moreover, the model successfully predicted the 3-fold behavioral periodicity of human participants.

Results

Construction of a conceptual object space

A novel 3D object, named greeble (Gauthier and Tarr, 1997; Fig.1a), was used to construct a conceptual object space. Within this space, locations were represented a series of unique greeble variants characterized by distinct length of their two components, namely "Loogit" and "Vacso," both of which formed the two dimensions of the space. The greeble in the center of the space was the prototype, serving as the target. In each trial, a greeble variant, randomly selected from the periphery of the space, was presented on screen (Fig.1b). Participants adjusted the length of Loogit and Vasco independently via button press to match the prototype as accurately as possible. This

process generated a navigational path constituted by a sequence of selected greeble variants (Fig.1c). To ensure comprehensive exploration of the object space, greeble variants were evenly sampled such that participants experienced conceptual directions ranged from 0° to 360° relative to the goal-location (i.e., the orange locations in Fig.1c; see Methods for details). Note that no participant was aware of the existence of the object space or had a subjective feeling of navigating during the experiment. To mitigate the impact of learning effects on BOLD signal series of MRI scanning, participants were trained one day prior to the MRI experiment (see Fig.S1 for details). As a result, all participants performed the task well, and the probability density map of the ending-locations across trials and participants showed the peak at the prototype (Fig. 1d).

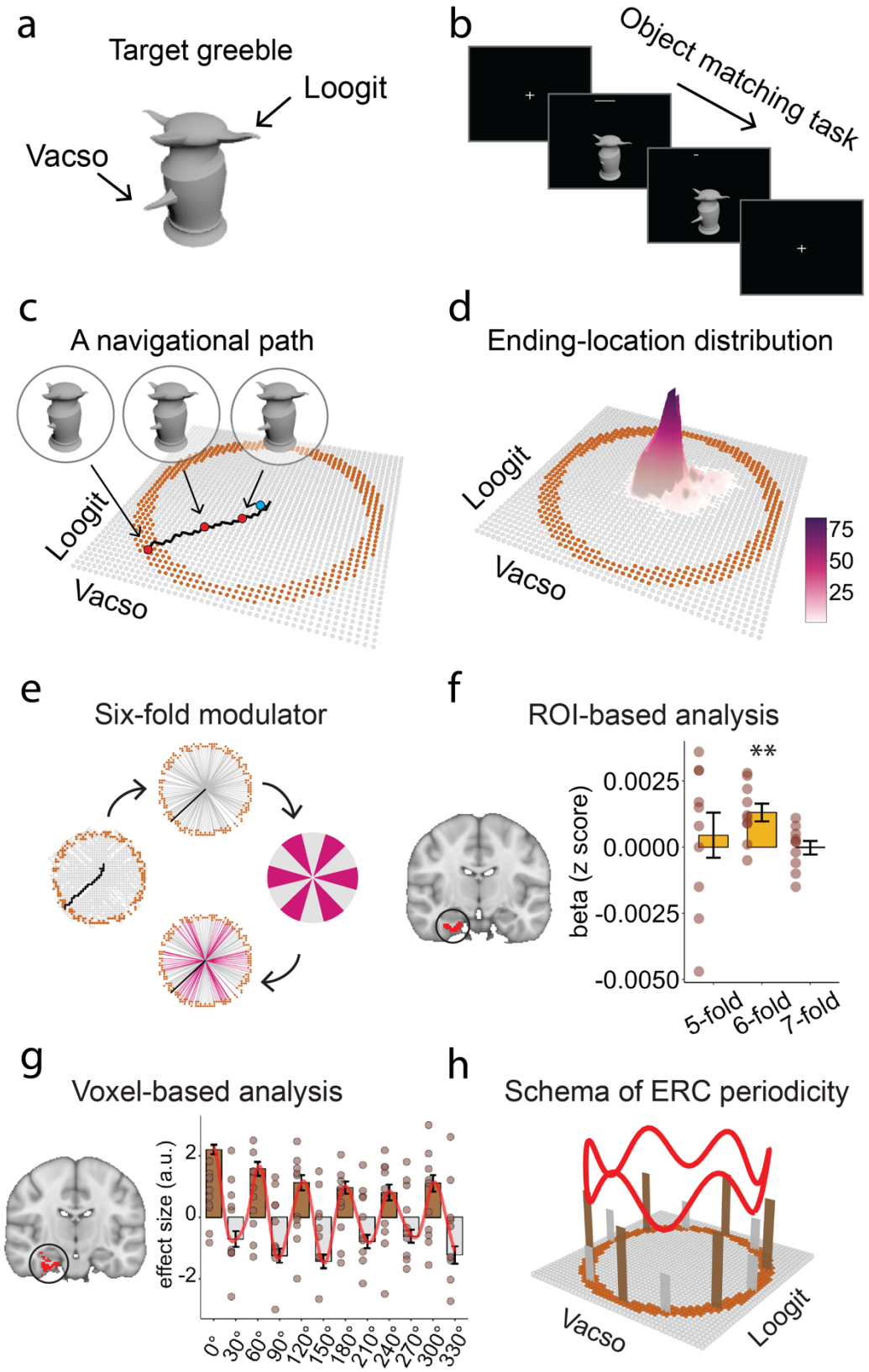
a
Target greeble
Loogit
Vacso
b
Object matching task
c
A navigational path
Loogit
Vacso
d
Ending-location distribution
Loogit
Vacso
75
50
25
e
Six-fold modulator
f
ROI-based analysis
**
0.0025
0.0000
-0.0025
-0.0050
beta (z score)
5-fold
6-fold
7-fold
g
Voxel-based analysis
2
0
-2
effect size (a.u.)
0°
30°
60°
90°
120°
150°
180°
210°
240°
270°
300°
330°
h
Schema of ERC periodicity
Vacso
Loogit

Figure 1. Experimental design and 6-fold modulation in the Entorhinal cortex. a) Depiction of the greeble prototype and its two defining components, namely "Loogit" and "Vacso." b) Within the MRI scanner, participants continuously adjusted the length of Loogit and Vacso to match the prototype by button press within a 10-s time limit. c) Conceptual object space. Each orange dot within the ring-shaped area represents a variant greeble, while the central blue dot indicates the prototype greeble (i.e., the goal-location). Red dots denote intermediate locations along the navigational path (i.e., the black line). d) Distribution of the ending-locations, aggregated across participants. e) Schematic detailing the 6-fold modulator for localizing grid cell activity. Participants' paths were simplified to straight lines connecting the starting and the ending-locations, which were further classified into either "aligned" or "misaligned" conditions. For each participant's individual path, see Fig. S2. f) ROI-based analysis, with an anatomical mask manually delineated from the MNI template, replicated the 6-fold modulation of BOLD signal series in comparison to both 5- and 7-fold modulations. g) Voxel-based sinusoid analysis revealed grid cell activity within the right ERC (peak MNI coordinate: 19, -15, -27; peak $t = 4.58$). h) Three-dimensional schema illustrating the relationship between the 6-fold modulation in the ERC and conceptual directions within the object space.

6-fold modulation in the ERC and 3-fold modulation in the HPC

In the fMRI analysis, we first identified the entorhinal hexagonal activity when participants implicitly navigated in the object space. With the sinusoidal analysis (Fig.1e, see Methods for details), we revealed a significant deviation from uniform grid orientations (Fig.S3, $p < 0.05$, Rayleigh test of uniformity, Bonferroni corrected), and identified a significant activity cluster in the right ERC (Fig.1g; $p < 0.01$, initial threshold; $p < 0.05$, small-volume cluster-corrected (SVC) for multiple comparisons; Cohen's $d = 0.7$), corresponding to the 6-fold modulation of the hexagonal pattern of grid cells, characterized by a 60° periodicity. In contrast, no significant clusters were detected corresponding to either 5-fold (72° periodicity) or 7-fold (51.4° periodicity) modulation. An additional ROI analysis with the anatomical ERC mask corroborated the robustness of the 6-fold modulation (Fig.1f, $t(9) = 3.89$, $p = 0.003$; Cohen's $d = 1.2$), not the 5- or 7-fold modulations (Fig.1f, 5-round: $t(9) < 1$, 7-round: $t(9) < 1$). These results confirmed the involvement of entorhinal grid cells in the object space where the object-matching task occurred, consistent with previous findings (e.g., Doeller et al., 2010, Constantinescu et al., 2016; Bao et al., 2019; Wagner et al., 2023; Raithel et al., 2023).

Anatomically, the HPC receives afferent projections from the ERC (Witter and Amaral, 1991; van Groen et al., 2003; Garcia and Buffalo, 2020), suggesting a potential for observing periodical neural activity patterns in the HPC because of the neural periodicity in the ERC. To test this intuition, our experimental design mandated that participants explored the full range of conceptual directions, ranged from 0° to 360° in increments of 1°, allowing the examination of hippocampal spatial periodicities of neural activities in addition to the established 60° periodicity. Specifically, we employed spectral analysis (see Methods for detail), which obviates the need for the prior hypothesis on periodicities or phase-offset calibrations as necessitated by the sinusoid analysis (Doeller et al., 2010; Constantinescu et al., 2016; Bao et al., 2019; Wagner et al., 2023; Raithel et al., 2023), to explore periodicity spectrum within the medial temporal lobe (MTL). In this analysis, conceptual directions were down-sampled into 15° bins, generating a vector of resampled directions (e.g., 0°, 15°, and 30°), thereby enabling the detection of frequencies up to 11 Hz. A Fast Discrete Fourier Transform (FFT) was performed on the direction-dependent activity series, as estimated by GLM and sorted in ascending order (Fig.2a). Spectral power was then extracted for each voxel, ranging from 0 Hz to 11 Hz. As a result, we observed a significant cluster with an FFT magnitude centered at 3 Hz within the anterior portion of the right HPC (Fig.2b;

$p < 0.05$, initial threshold; $p < 0.05$, SVC for multiple comparisons; Cohen's $d = 0.9$). Visual inspection further indicated that this peak magnitude at 3 Hz was presented in the CA1 region of the HPC. Additionally, the direction-dependent activity series, extracted via an anatomical mask of the anterior HPC, showed a discernible 3-fold periodic neural activity pattern that fluctuates as a function of conceptual directions (Fig.2c & d). The 3-fold modulation in the HPC was not due to the down-sampling of directions into 15° bins, as this finding was reliably observed when using both 10° and 20° bins (Fig. S4). Taken together, our spectral analysis successfully identified a robust 3-fold periodicity located in the CA1 region of the HPC.

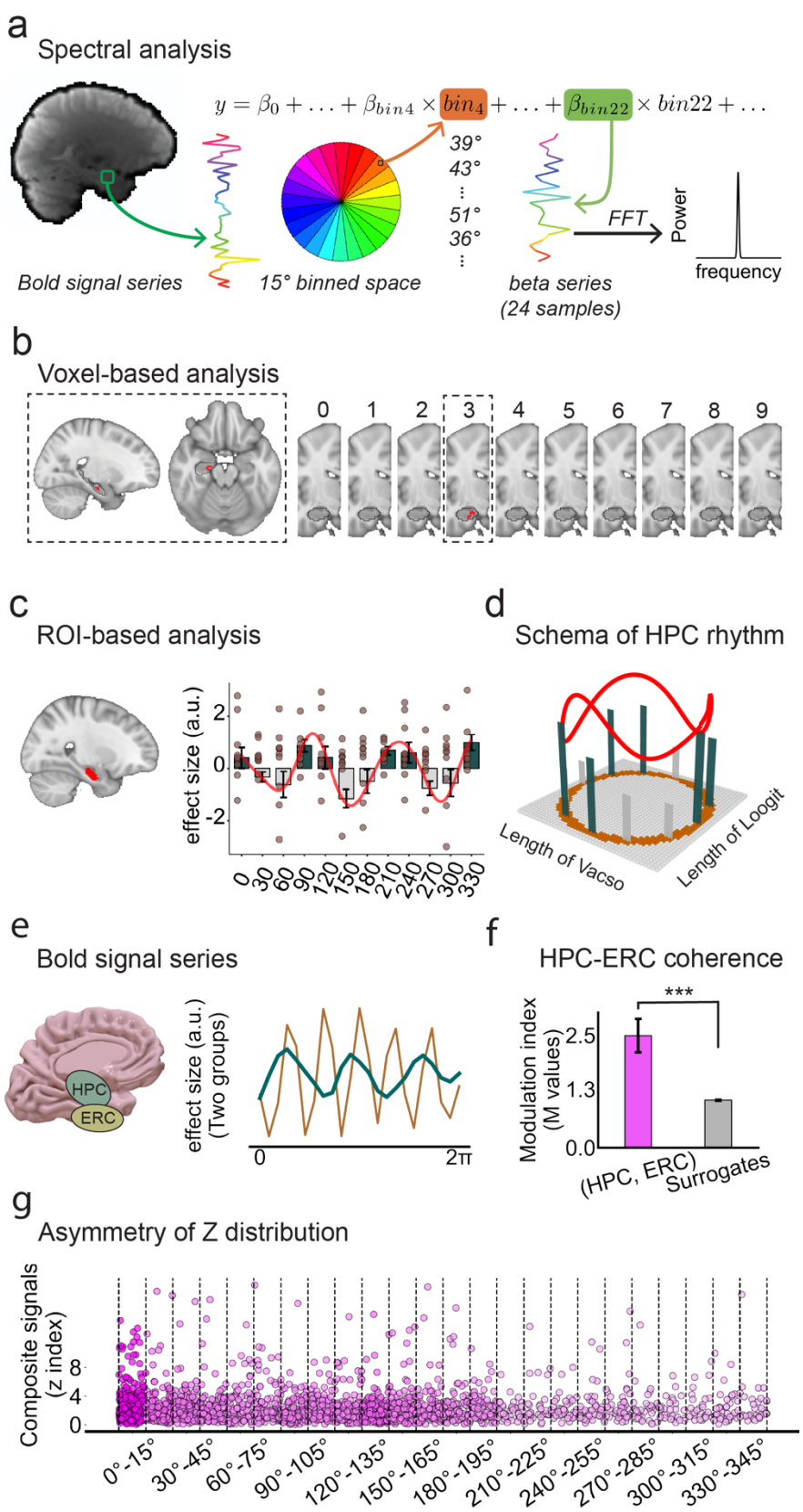
a
Spectral analysis
$y = \beta_0 + \ldots + \beta_{bin4} \times bin_4 + \ldots + \beta_{bin22} \times bin22 + \ldots$
39°
43°
51°
36°
FFT
Power
frequency
Bold signal series
15° binned space
beta series
(24 samples)
b
Voxel-based analysis
0 1 2 3 4 5 6 7 8 9
c
ROI-based analysis
effect size (a.u.)
2
0
-2
0 30 60 90 120 150 180 210 240 270 300 330
d
Schema of HPC rhythm
Length of Vacso
Length of Loogit
e
Bold signal series
HPC
ERC
effect size (a.u.)
(Two groups)
0
2π
f
HPC-ERC coherence
***
Modulation index
(M values)
2.5
1.3
0.0
(HPC, ERC)
Surrogates
g
Asymmetry of Z distribution
Composite signals
(z index)
8
4
0
0°-15°
30°-45°
60°-75°
90°-105°
120°-135°
150°-165°
180°-195°
210°-225°
240°-255°
270°-285°
300°-315°
330°-345°

Figure 2. 3-fold modulation in the HPC and its synchronization with 6-fold modulation in the ERC. a) Schema illustrating the procedure of spectral analysis to identify neural periodicities within the MTL. b) Voxel-based spectral analysis revealed a significant 3-fold modulation in the right HPC (Peak MNI coordinate: 20, -14, -18). c) The 3-fold modulation of the HPC based on the anatomical mask of bilateral HPC. d) Three-dimensional schema illustrating the relationship between the 3-fold modulation in the HPC and conceptual directions within the object space. e) Visual inspection on the averaged BOLD signal series, extracted from anatomical masks of the HPC (green) and the ERC (yellow), showed a phase-locked pattern. f-g) Amplitude-phase coupling analysis on the ERC and HPC activity series corroborated the significant coherence of HPC and ERC activity series, suggested by f) the significantly higher modulation index M (purple) as compared to that of surrogates (gray) and g) the asymmetric distribution of composite z values as a function of movement directions. Note that the probability density (denoted by the color scale of purple) showed the strongest density (darker purple) at the 0°-15° bin, consistent with the observation of the phase shift. Error bars indicate SEM. ***: $p < 0.001$

The hippocampal 3-fold modulation has not been previously reported in the spatial domain either by neurophysiological or fMRI studies. To validate the reliability of this finding, we therefore recruited a completely new group of participants (i.e., the replication group) and conducted the experiment at a different imaging center. The experimental design, data preprocessing and analyses remained identical with the original experimental group. In short, we replicated all major findings reported earlier (Fig.S5). That is, we found the involvement of grid cells in the right ERC (Fig.S5a, $p < 0.01$, initial threshold; $p < 0.05$, SVC for multiple comparison; Cohen's $d = 0.7$), and more importantly identified the 3-fold modulation in the CA1 region of the right HPC (Fig.S5b, $p < 0.05$, initial threshold; $p < 0.05$, SVC for multiple comparison; Cohen's $d = 3.3$). The results in the replication study substantiate the reliability of the 3-fold modulation observed in the HPC.

To further explore the hypothesis that the observed periodic neural activity in the HPC may originate from the periodic activity of grid cells in the ERC, we investigated whether the phases of these two periodic activities were synchronized. To do this, we extracted the BOLD signal series from each of the ERC and HPC of each participant, using data derived from the sinusoid and spectral analyses, respectively. Visual inspection shows that 80% of the participants exhibited

discernible phase-locked patterns (Fig.S6), characterized by the overlapping peaks of 3-fold and 6-fold periodicities (Fig.2e). To corroborate the observation, an amplitude-phase modulation analysis was employed to quantify the extent of cross-frequency coherence between the ERC and HPC. Specifically, the amplitude envelope from high-frequency activity series in the ERC and the phase of low-frequency activity series in the HPC were extracted. The composite signal z was constructed at each sample point through $z = A_{ERC}e^{i\phi_{HPC}}$ (Canolty et al., 2006). The modulation index M was derived by computing the mean of vector Z for the composite signal series and permutated surrogates of each participant. This analysis revealed a significantly higher modulation strength relative to surrogate controls (Fig. 2f; $t(19) = 3.77$, $p < 0.001$), suggesting a phase coherence between the ERC and HPC. Moreover, the radial asymmetry, observed from the probability density function of Z indices, signifies the presence of shared mutual information encoded in specific phases (i.e., movement directions) between the ERC and HPC (Fig.2g). Notably, the highest density of Z indices was found within the 0°-15° bin ($p < 0.05$, corrected for multiple comparisons), fitting nicely with the observed phase shift shown in Fig. 2e. Taken together, both visual inspection and statistical analyses indicate that peaks in the ERC activity series selectively aligned with those in the HPC activity. Note that this result differs from prior work in the temporal domain, where neural activity coherence is typically characterized by the modulation of low-frequency bands on high-frequency signals (e.g., Buzsaki, 2006; Maris et al., 2011; Friese et al., 2013). Rather, our results suggest a potential causal link between the formation of 3-fold periodicity of hippocampal place cells and the 6-fold periodicity of entorhinal grid cells, despite pronounced individual differences in the phase of activity series across participants (Fig.S6).

The "E-H PhaseSync" Model

To elucidate the mechanism by which the hexagonal patterns of entorhinal grid cells project onto the HPC to give rise to the 3-fold periodicity and further guides the navigation, we developed a computational model, termed the "E-H PhaseSync" model. This model is predicated on an intuition that the 3-fold periodicity may be intrinsically linked to the three primary axes of the hexagonal firing pattern of grid cells through a process of phase-locking. This intuition is inspired by three key neuroscience findings. First, the near-invariance characteristics of grid orientation and spacing (Hafting et al., 2005; Stensola et al., 2015; Krupic et al., 2015; Gardner et al., 2022) suggest that

downstream cortical areas who receive grid codes may fluctuate as a function of spatial orientations due to the three primary axes of the hexagonal pattern. Second, vector trace cells in the subiculum of the HPC, which show trace fields in representing location sequences (Tsao et al., 2013; Bicanski and Burgess, 2018; Bicanski and Burgess, 2020; Poulter et al., 2021), receive projections from grid cell populations (Naber et al., 2001) and convey information to the CA1 of the HPC (Sun et al., 2019) where place cells reside. Third, the grid cell activity, which is structured by spatial orientations, can be reliably elicited by movement directions (Doeller et al., 2010; Constantinescu et al., 2016; Nau et al., 2018; Bao et al., 2019; Wagner et al., 2023), suggesting that spatial orientations might underpin the formation of directions. Therefore, in the E-H PhaseSync model, projections from entorhinal grid cells are designated to establish the 3-fold periodicity of the HPC via the ERC-HPC circuit (Fyhn et al., 2007; Hales et al., 2014), and then the 3-fold modulation serves as a periodic scaffold that embeds path directions in hippocampal vector field to support navigation (Fig. 3).

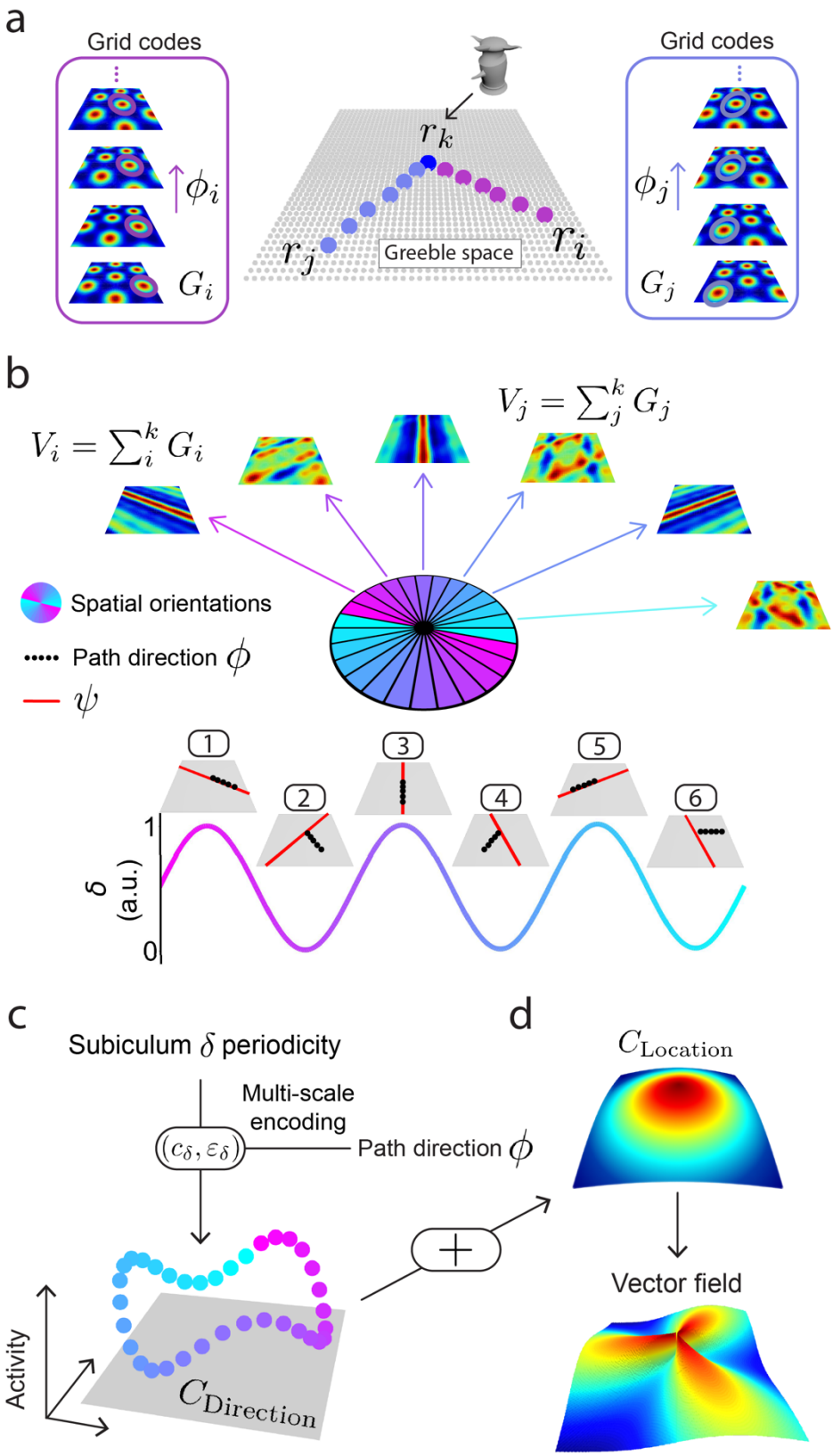
a
Grid codes
ϕ_i
G_i
r_k
r_j
r_i
Greeble space
Grid codes
ϕ_j
G_j
b
$V_i = \sum_i^k G_i$
$V_j = \sum_j^k G_j$
Spatial orientations
Path direction ϕ
ψ
1
2
3
4
5
6
1
0
δ (a.u.)
c
Subiculum δ periodicity
Multi-scale encoding
$(c_\delta, \varepsilon_\delta)$
Path direction ϕ
Activity
$C_{\text{Direction}}$
d
C_{Location}
Vector field

Figure 3. The E-H PhaseSync Model. a) Discrete location map by entorhinal grid cells. Paths from location r_i and r_j to the goal-location r_k in the object space are planned by imagination, which either aligns or misaligns with grid orientations, respectively. During path planning, entorhinal grid cells corresponding to the locations along the envisaged paths are activated. Note that these grid codes differ in phase. b) Orientation map by subiculum vector trace cells. Vector trace fields V is formed by integrating the grid codes activated in the path, which is symmetrical for path direction ϕ and its opposite ϕ+180° relative to goal-location (i.e., the pie chart). The activation map δ of VTCs is quantified by the difference between spatial orientation ψ (i.e., the red line) and path direction ϕ' (i.e., ϕ mod 180° ; the dashed points). A large δ value, indicating a perfect match between ψ and ϕ (e.g., $\boxed{1}$ $\boxed{3}$ $\boxed{5}$), elicits stronger activation of vector trace cells. In contrast, a small δ value results from a mismatch between ψ and ϕ (e.g., $\boxed{2}$ $\boxed{4}$ $\boxed{6}$). Accordingly, activation of vector trace cell population illustrates a 3-fold scaffold with its peaks corresponding to grid orientations. c) Direction map by the hippocampal place cells. Place cells inherit the periodic scaffold of the orientation map δ defined by spatial frequency c_δ and phase ε_δ. The direction map $C_{Direction}$ is constructed by embedding path directions into the 3-fold scaffold through multi-scale encoding (Fig.S7). Color scale denotes path directions ranging from 0° to 360° . e) Vector map C. The vector map is constructed by integrating the hippocampal direction map $C_{Direction}$ with distance map $C_{Location}$.

In the E-H PhaseSync model, the entorhinal grid cell population consists of 2,025 grid cells, each uniquely configured with a spatial phase tied to a specific spatial location. All grid cells maintain a constant grid orientation (see Methods for details). Path direction ϕ is determined by mental imagination (Hasselmo, 2009; Buckner, 2010; Mullally and Maguire, 2014), which mentally maps out a path toward a goal-location r_k from a starting-location r within the object space (Fig.3a). This process, inspired by the "forward replay" observed in place cells, where an individual place cell triggers a sequence of spatially adjacent place cells (Diba and Buzsáki, 2007; Dragoi and Tonegawa, 2011; Pfeiffer, 2020), activates a group of grid cells that encode locations along path direction ϕ (Gardner et al., 2022). The linear combination of grid codes (i.e., hexagonal firing patterns of grid cells) along a path forms vector trace field V:

$$V_i = \sum_i^k G_i \tag{1}$$

where G_i denotes the grid code at location r_i (Fig. 3b). Note that when path direction ϕ_i perfectly aligns with one of the primary axes of grid cells, vector trace field V_i exhibits a "planar wave" pattern (Welday et al., 2011, Krupic et al., 2012) (Fig. 3b top left), whereas when misaligned, vector trace field V_j with an irregular multi-peak pattern is formed (Fig. 3b top right).

A vector trace cell in the subiculum receives the vector trace field derived from the populational coding of entorhinal grid cells, and then calculates spatial orientation ψ. When path direction ϕ aligns with one of grid orients, spatial orientation ψ aligns with the path direction (Fig. 3b; i.e., $\boxed{1}\boxed{3}\boxed{5}$). However, when misaligned, spatial orientation ψ deviates away from path direction ϕ (i.e., $\boxed{2}\boxed{4}\boxed{6}$). To quantify this deviated ψ, we first collect orientation selectivity for all possible orientations for the vector trace cell:

$$\Psi = \left\{\sum_R V_{\psi,R}\right\}_{\psi=0}^{\pi} \tag{2}$$

where R represents a path to the goal-location r_k given a certain spatial orientation ψ. Note that because vector trace field is symmetric relative to goal-location, spatial orientation ψ ranges from 0 to π. Accordingly, by pooling all spatial orientation ψ encoded by vector trace cell population in the subiculum, the object space is tessellated by spatial orientations ranging from 0 to π. To further determine spatial orientation ψ, an approach of winner-take-all dynamics (Bicanski and Burgess, 2019) is adopted:

$$\psi_j = \operatorname{argmax} \Psi_j \tag{3}$$

where ψ_j is the maxima of vector Ψ at location r_j. Critically, because spatial orientation ψ is largely determined by the degree of alignment between path direction ϕ and the primary axes of grid cell, a 3-fold periodicity (i.e., aligned, deviated; aligned, deviated; aligned, deviated) emerges in this orientation map (Fig. 3b bottom). To quantify the difference between spatial orientation ψ and path direction ϕ, the activation magnitude of vector trace cells δ is defined by $|\psi - \phi \ mod \ \pi|$. A small δ value indexes a close match between spatial orientation and path direction (e.g. ψ=ϕ), whereas a large δ value results from a mismatch between ψ and ϕ (e.g. $\psi \neq \phi$). To align with conventional usage, smaller δ values are normalized with larger activation magnitudes and vice versa (Equation 8). Accordingly, the activity of vector trace cell population shows a 3-fold periodicity with its peak responses (i.e., $\boxed{1}\boxed{3}\boxed{5}$), which provides the spatial periodic scaffold for CA1 place cells.

With this periodic scaffold, path direction ϕ is no longer the movement direction at each location, unless it aligns with grid orientations. Therefore, movement direction θ_j at the location r_j, which is represented by a CA1 place cell corresponding to this location, is jointly determined by three factors: the path direction ϕ_j from r_j to goal-location r_k, the magnitude of the 3-fold periodicity c_δ inherited from vector trace cell population, and the spatial phase ε_δ representing grid orientation:

$$\theta_j = \cos\left(c_\delta \times \arctan\left(\phi_j\right) + \varepsilon_\delta\right) \tag{4}$$

where θ_j is the movement direction at the location r_j represented by a CA1 place cell. Accordingly, by pooling all movement direction θ encoded by CA1 place cell population, the object space is tessellated by movement directions in the HPC ranging from 0 to 2π, forming hippocampal direction map $C_{Direciton}$ (Fig.3c). Because the direction map inherits the 3-fold periodic scaffold from vector trace cells in the subiculum, a 3-fold periodicity is also present in hippocampal direction map.

In the final stage of the model, by linearly summing hippocampal distance map $C_{Location}$ that signifies the distance from locations in the object space to the goal-location (Bush et al., 2015), hippocampal direction $C_{Direction}$ evolves into hippocampal vector field C (Fig.3d):

$$C = C_{Diretion} + C_{Location} \tag{5}$$

Where vector field C serves as direction-guiding vector field, leading from any location within the object space towards the goal-location (Ormond and O'Keefe, 2022). That is, during the process

of path integration, any movement transition is determined by the strongest activity of C_r surrounding the self-location r.

3-fold modulation on behavior performance

The E-H PhaseSync model provides a plausible explanation on the origin of the 3-fold spatial periodicity observed in the HPC, and further implies its critical role in path integration. To validate whether the 3-fold spatial periodicity indeed impacts navigation behavior, we implemented the E-H PhaseSync model in an agent to perform a path integration task, where the agent continuously received its current location (i.e., self-location) as input and generated the subsequent movements in the object space until reaching the goal. A total of 156 trials were completed. Interestingly, we observed that the agent's paths integrated from movement directions displayed an anisotropic pattern in the object space, characterized by a clear 3-fold periodicity (Fig.4a). To further quantify this pattern, we calculated each path's length by summing the distances of all movements within a trial, and found a 3-fold fluctuation in path length, correlating with movement directions ranged from 0° to 360° (Fig.4b). Spectral analysis further confirmed the significance of 3-fold periodicity (Fig.4c, red arrow; $p < 0.05$, corrected for multiple comparisons), and no significant spectral power was detected for other periodic modulations (Fig.4c). That is, contrary to the commonly held assumption of isotropic performance across movement directions, our findings indicate that agents tend to perform more efficiently (i.e., travel shorter distances) when the spatial orientation between the start- and goal-locations aligns with grid axes compared to misalignment. Therefore, agents' navigation performance is influenced by the spatial periodicity of the HPC, which in turn derive from periodic activation patterns of entorhinal grid cells.

Model prediction

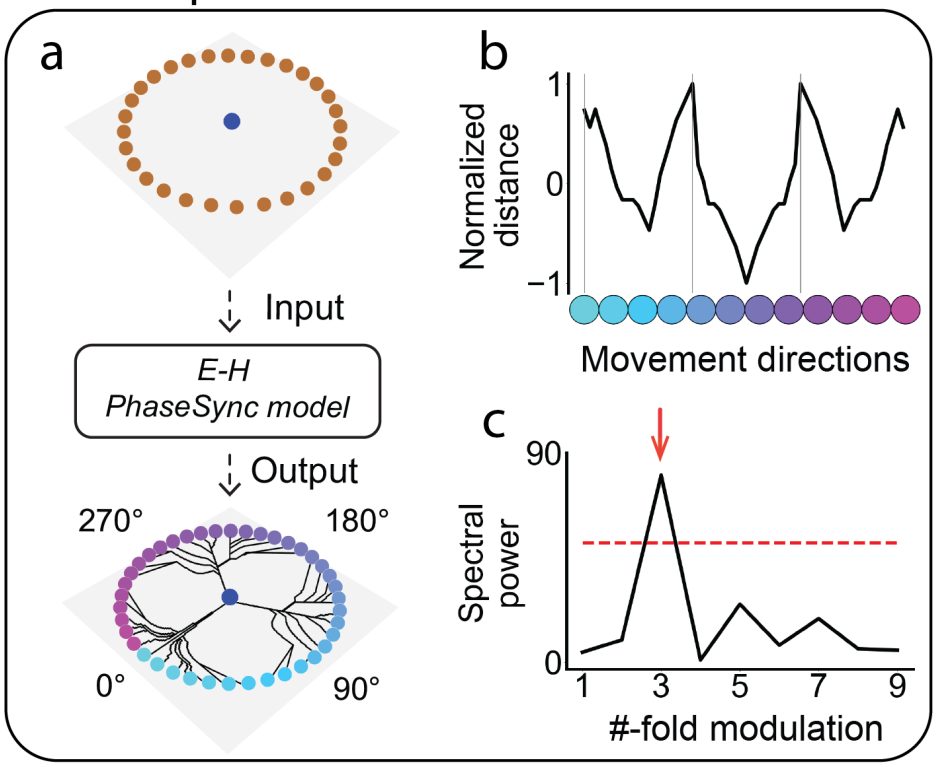

Human behavior

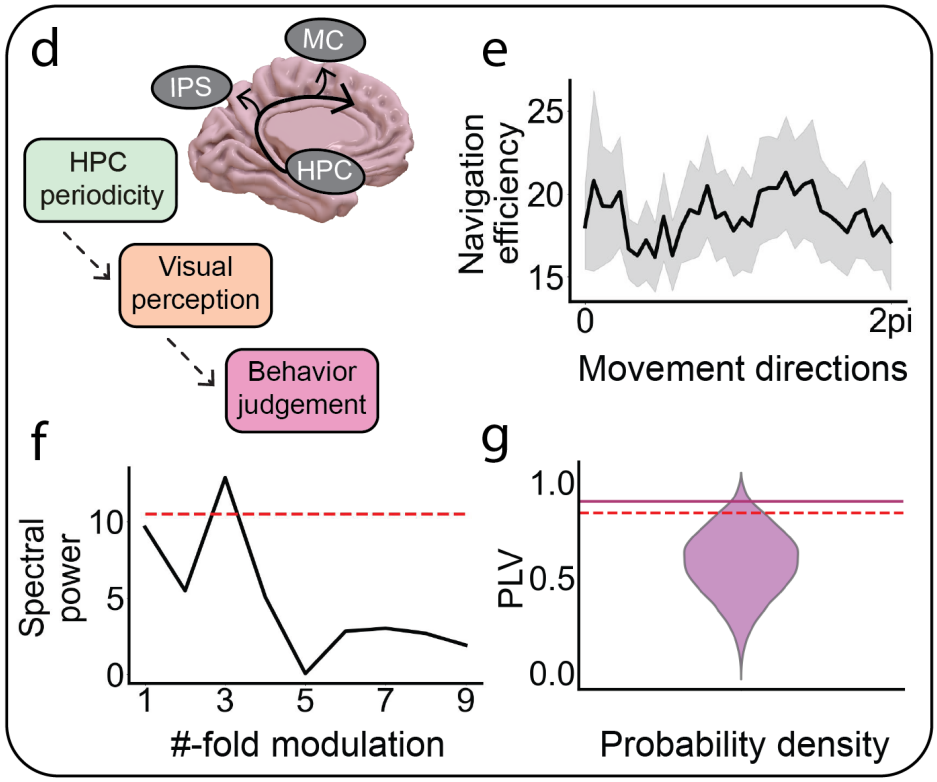

Figure 4. The impact of 3-fold periodicity on behavior performance. a) Implementation of the E-H PhaseSync model. Starting-locations were arranged in a ring around the central goal, mirroring the fMRI experiment setup. In a trial, the agent, equipped with the model, moved from its starting-location to a new location, as generated by the model using the starting-location as input. Upon reaching this new location, the agent updated the starting-location. This cycle repeated until the goal was reached. The agent's paths, integrated from movement directions, displayed an anisotropic pattern in the object space. Color in the ring denotes movement directions ranged from 0° to 360°. b) Agent's behavioral performance. The agent's navigation efficiency, which was measured by the distance traveled from the starting- to goal-locations, fluctuated as a function of movement directions. Note that the agent achieved maximum efficiency (i.e., the shortest travel distance) when its movement directions aligned with one of the primary axes of grid codes (i.e., the gray vertical lines). The y-axis denotes the normalized distance, and the x-axis shows the movement directions. c) 3-fold modulation of agent performance. Spectral analysis revealed the 3-fold modulation in navigation ($p<0.05$, corrected for multiple comparisons). The red dashed line indicates the baseline derived from permutation. The red arrow denotes the peak of the power spectrum. d) Visuomotor brain circuit potentially inheriting HPC's 3-fold modulation. IPS: Intra Parietal Sulcus; MC: Motor Cortex. e) Humans' navigation efficiency, which was measured by a composite index of path length and deviation from the goal- to ending-locations, fluctuated as a function of movement directions. The shaded area denotes SE. f) 3-fold modulation of human performance. Spectral analysis revealed significant spectral power at 3-fold ($p<0.05$, corrected for multiple comparisons). The red dashed line denotes the baseline derived from permutation. g) Human performance phase-locked with hippocampal BOLD signals. Phase-Locking Value (PLV, purple line) exceeded the threshold (red dashed line) of the 95th percentile of the PLV distribution obtained from randomly shuffled surrogates at 3-fold periodicity ($p<0.05$, corrected for multiple comparisons).

A more challenging examination of the E-H PhaseSync model's validity is whether spatial periodicity is evident in humans' navigation behavior, which, to our knowledge, has not been reported yet. Considering the anatomy of the visual-motor system in the brain, it is plausible that hippocampal periodic activity may propagate to egocentric cortical areas such as the precuneus and the lateral parietal cortex, hereby influencing visuospatial decision in navigation (Fig. 4d). To

explore spatial periodicity in human navigation, we evaluated participants' navigation efficiency using two metrics: path length and error size between the goal- and the actual ending-location (see Methods for details), as participants seldom stopped exactly at the goal-location. Better navigation efficiency was indexed by the composite score of shorter travel lengths and smaller error size. We found that average navigation efficiency fluctuated as a function of movement directions, showing an approximate 3-fold modulation pattern (Fig. 4e). Spectral analysis confirmed the significance of this behavioral periodicity in humans with a spectral power peak at 3-fold (Fig. 4f; $p < 0.05$, corrected for multiple comparisons). To further illustrate the causal relationship between hippocampal and behavioral periodicities, we calculated the phase-locking coherence across participants for each of 0- to 17-fold (i.e., half of the sample size). The result found that the Phase-Locking Value (PLV) at 3-fold significantly higher than the shuffled control (Fig.4g; $p < 0.05$, corrected for multiple comparisons), suggesting that the human behavioral periodicity likely derives from the hippocampal periodicity.

In summary, the spatial periodicity identified in both the agent's and humans' navigation behavior align nicely with the E-H PhaseSync model's prediction, thereby supporting the model as a mechanistic framework that integrates the ERC and HPC as a whole through phase synchronization during navigation.

Discussion

Path integration, the process of acquiring spatial knowledge from one moment to the next one in both physical (Wang and Spelke, 2002; Gallistel, 2017) and conceptual spaces (Epstein et al., 2017; Behrens et al., 2018; Park et al., 2020), is realized especially by the HPC and ERC of the hippocampal complex. However, given that these two regions perform distinct functions, with entorhinal grid cells encoding continuous space discretely (Hafting et al., 2005) and hippocampal place cells represent localized spatial locations (O'Keefe and Dostrovsky, 1971), a longstanding puzzle is to understand how these two regions work collaboratively in path integration. Through both empirical experiments and computational modeling, we identified a 3-fold spatial periodicity in the CA1 area of the HPC, confirming the existence of hippocampal vector fields at the population level. Critically, the periodicity's phase was synchronized with the 6-fold spatial periodicity in the ERC. Inspired by this empirical finding, we proposed the E-H PhaseSync model

526 to elucidate how hippocampal vector fields were formed by constructing the 3-fold scaffold to
527 accommodate movement directions in the HPC from the entorhinal grid codes. Further, this
528 hippocampal periodic activity likely propagated to egocentric cortical areas within the visual-
529 motor system, which eventually introduced a 3-fold spatial periodicity into navigation
530 performance. In summary, our results offer a mechanistic framework that integrates the ERC and
531 the HPC through phase synchronization in performing path integration for navigation.

532 Navigational models (e.g., Banino et al., 2018; Gao et al., 2018; Bicanski and Burgess,
533 2019; Whittington et al., 2020; Edvardsen et al., 2020) heavily rely on simulations of hippocampal
534 and entorhinal cells. However, the computational principles governing how these cells operate
535 collaboratively as an integrated whole are not fully understood. Our fMRI experiment provides
536 reliable empirical evidence suggesting the principle of spatial periodic computation, which embeds
537 spatial orientations and path directions within a periodic scaffold defined by 3-fold spatial
538 periodicity and spatial phase (i.e., grid orientation). Furthermore, the finding that the behavioral
539 periodicity in navigation is phase-coupled with the hippocampal periodicity suggests that this
540 periodic scaffold may extend its function to downstream cortical regions beyond the MTL (see
541 also Bieri et al., 2014; Fiebelkorn et al., 2018). In parallel, neurons exhibiting spatial selectivity in
542 upstream cortical regions, possibly first reported by Hubel and Wiesel (1959; 1962) for the
543 ganglion cells in representing visual locations, may also provide external visual cues with local
544 geometry to the HPC, especially when allocentric map is not accessible (Gallistel, 2017; Julian et
545 al., 2018; Keinath et al., 2017). Taken together, the principle of spatial periodic computation may
546 serve as a general rule for structuring information in both spatial and temporal domains throughout
547 the brain, possibly facilitating how information is organized, stored, and retrieved as a structured
548 entity.

549 Based on this principle, we proposed the E-H PhaseSync model to elucidate how the 3-fold
550 periodicity was generated by populational neurons within the ERC-HPC circuit and its role in
551 supporting the encoding of movement directions by hippocampal place cells (McNaughton et al.,
552 1983; Muller et al., 1994; Leutgeb et al., 2000; Rubin et al., 2014; Meister and Buffalo, 2016; Sarel
553 et al., 2017; Ormond and O'Keefe., 2022). A key component of this model is the representation of
554 spatial orientation, which acts as a bridge between the global spatial metric of entorhinal grid cells
555 and the local movement directions of hippocampal place cells. Specifically, this component
556 transforms spatial metric encoded in an abstract cognitive map into movement directions in an

actual one, hereby enabling agents' navigation in both physical and conceptual spaces. The representation of spatial orientation in the model aligns nicely with the planar waves from the "grid cell to place cell" model (Solstad et al., 2006; De Almeida et al., 2009; Bush et al., 2014; Bush et al., 2015; Bicanski and Burgess, 2019), the oscillatory interference theory (Welday et al., 2011), and the concept of the spatially periodic bands (Krupic et al., 2012). In addition, it offers an explanation for the observation of irregular trace fields (Tsao et al., 2013; Poulter et al., 2021) by suggesting the cause of the misalignment between the primary axes of grid cells and path directions encoded by place cells. Furthermore, the symmetric characteristic of spatial orientation representation may elucidate an interesting phenomenon observed in reorientation studies (Hermer and Spelke, 1994; Julian et al., 2015; Julian et al., 2018), where rodents and young children tend to search for targets equally at both the rewarded and geometrically equivalent opposite locations. While the E-H PhaseSync model holds promising at algorithmic level, there is a notable lack of direct neural evidence supporting it, especially concerning the representation of spatial orientation. The recent discovery of vector trace cells in the subiculum (Tsao et al., 2013; Bicanski and Burgess, 2018; Bicanski and Burgess, 2020; Poulter et al., 2021), which help forming a vector or gradient path from one location to another, suggests a potential neural basis in representing spatial orientations. Further neurophysiological investigations are needed to unveil their exact role and mechanism. Another limitation of this model is its incapability to address how hippocampal vector fields adapt within context-specific scenes during learning. For example, it does not elucidate how vector fields update in response to unexpected landmark or obstacles. A possible mechanism could involve the ERC receiving contextual information and updated goal identities (e.g., intermediate landmarks) from the parahippocampal and perirhinal cortices (Eichenbaum and Lipton, 2008; Montaldi and Mayes, 2010; Wilson et al., 2013). Then, this information might be integrated into environmental metric (Stensola et al., 2015; Bottini and Doeller, 2020) through the excitation-inhibition dynamics (Amari, 1977; Samsonovich and McNaughton, 1997; Fuhs and Touretzky, 2006; Burak and Fiete, 2009; Couey et al., 2013). Thus, further biologically plausible models, which explore interactive principles of various cognitive maps that flexibly organize past experiences for the future (Zhang et al., 2023), are needed to be built in the implementation level, which may provide further insights how these maps contribute to a unified and efficient representation of the external world (VanRullen and Kanai, 2021).

Data availability

The data that support the findings of the present study are available from the corresponding author (J.L.) upon request.

Code availability

All analyzes reported in the present study were conducted with the customized codes written in Python (version 3.9), Pygame (version 2.0), Matlab (version 2019b), R (version 4.0), and GNU bash (version 3.2.57). The codes will be available from the corresponding author (J.L.) upon request. The neuroimaging toolbox and machine learning framework used by the present work are publicly available as following: FreeSurfer (v7.1, https://surfer.nmr.mgh.harvard.edu/), FSL (version 6.0, https://fsl.fmrib.ox.ac.uk/fsl/fslwiki;), and Torch (version 1.9, https://pytorch.org/).

Acknowledgments

We gratefully acknowledge Mr. Yue Wu and Ms. Yuannan Li for helpful discussions during data analysis, Prof. Russell Epstein for valuable comments on fMRI results of and computational modelling, and Dr. Michael Tarr for sharing the code for greeble stimulus generation. Computational work was supported by High-performance Computing Platform of Peking University. The work was supported by the National Key R&D Program of China (2020AAA0105200), China Postdoctoral Science Foundation (2022M710470), Beijing Municipal Science & Technology Commission & Administrative Commission of Zhongguancun Science Park (Z221100002722012), Tsinghua University Guoqiang Institute (2020GQG1016), and Beijing Academy of Artificial Intelligence (BAAI).

Conflict of interest

None declared

Author Contributions

J.L. conceived the study and provided advice. B.Z. conducted the fMRI study, performed the analysis, and built the computational model. B.Z. and J.L. wrote the paper.

Reference

Amari, S. (1977). Dynamics of pattern formation in lateral-inhibition type neural fields. Biol Cybern, 27(2), 77-87. https://doi.org/10.1007/BF00337259

Buzsaki, G. (2006). *Rhythms of the Brain*. Oxford university press.

Burgess, N., Barry, C., & O'Keefe, J. (2007). An oscillatory interference model of grid cell firing. Hippocampus, 17(9), 801-812. https://doi.org/10.1002/hipo.20327

Blair, H. T., Welday, A. C., & Zhang, K. (2007). Scale-invariant memory representations emerge from moire interference between grid fields that produce theta oscillations: a computational model. Journal of Neuroscience, 27(12), 3211-3229.

Burak, Y., & Fiete, I. R. (2009). Accurate path integration in continuous attractor network models of grid cells. PLoS Comput Biol, 5(2), e1000291. https://doi.org/10.1371/journal.pcbi.1000291

Buckner, R. L. (2010). The role of the hippocampus in prediction and imagination. *Annual review of psychology*, *61*, 27-48.

Bush, D., Barry, C., & Burgess, N. (2014). What do grid cells contribute to place cell firing? Trends Neurosci, 37(3), 136-145. https://doi.org/10.1016/j.tins.2013.12.003

Bieri, K. W., Bobbitt, K. N., & Colgin, L. L. (2014). Slow and fast gamma rhythms coordinate different spatial coding modes in hippocampal place cells. Neuron, 82(3), 670-681. https://doi.org/10.1016/j.neuron.2014.03.013

Bush, D., Barry, C., Manson, D., & Burgess, N. (2015). Using grid cells for navigation. Neuron, 87(3), 507-520. https://doi.org/10.1016/j.neuron.2015.07.006

Behrens, T. E., Muller, T. H., Whittington, J. C., Mark, S., Baram, A. B., Stachenfeld, K. L., & Kurth-Nelson, Z. (2018). What is a cognitive map? Organizing knowledge for flexible behavior. Neuron, 100(2), 490-509.

Bicanski, A., & Burgess, N. (2018). A neural-level model of spatial memory and imagery. Elife, 7, e33752.

Banino, A., Barry, C., Uria, B., Blundell, C., Lillicrap, T., Mirowski, P., ... & Kumaran, D. (2018). Vector-based navigation using grid-like representations in artificial agents. Nature, 557(7705), 429-433.

Bush, D., & Schmidt-Hieber, C. (2018). Computational models of grid cell firing. Hippocampal Microcircuits: A Computational Modeler's Resource Book, 585-613.

Bicanski, A., & Burgess, N. (2019). A computational model of visual recognition memory via grid cells. Current Biology, 29(6), 979-990.

Bao, X., Gjorgieva, E., Shanahan, L. K., Howard, J. D., Kahnt, T., & Gottfried, J. A. (2019). Grid-like Neural Representations Support Olfactory Navigation of a Two-Dimensional Odor Space. Neuron, 102(5), 1066-1075 e1065. https://doi.org/10.1016/j.neuron.2019.03.034

Bicanski, A., & Burgess, N. (2020). Neuronal vector coding in spatial cognition. Nature Reviews Neuroscience, 21(9), 453-470.

Bottini, R., & Doeller, C. F. (2020). Knowledge across reference frames: Cognitive maps and image spaces. Trends in Cognitive Sciences, 24(8), 606-619.

Canolty, R. T., Edwards, E., Dalal, S. S., Soltani, M., Nagarajan, S. S., Kirsch, H. E., ... & Knight, R. T. (2006). High gamma power is phase-locked to theta oscillations in human neocortex. *science*, *313*(5793), 1626-1628.

Colgin, L. L., Moser, E. I., & Moser, M. B. (2008). Understanding memory through hippocampal remapping. *Trends in neurosciences*, *31*(9), 469-477.

Couey, J. J., Witoelar, A., Zhang, S. J., Zheng, K., Ye, J., Dunn, B., Czajkowski, R., Moser, M. B., Moser, E. I., Roudi, Y., & Witter, M. P. (2013). Recurrent inhibitory circuitry as a mechanism for grid formation. Nat Neurosci, 16(3), 318-324. https://doi.org/10.1038/nn.3310

Constantinescu, A. O., O'Reilly, J. X., & Behrens, T. E. J. (2016). Organizing conceptual knowledge in humans with a gridlike code. Science, 352(6292), 1464-1468. https://doi.org/10.1126/science.aaf0941

De Valois, R. L., Albrecht, D. G., & Thorell, L. G. (1982). Spatial frequency selectivity of cells in macaque visual cortex. Vision Res, 22(5), 545-559. https://doi.org/10.1016/0042-6989(82)90113-4

Diba, K., & Buzsáki, G. (2007). Forward and reverse hippocampal place-cell sequences during ripples. *Nature neuroscience*, *10*(10), 1241-1242.

De Almeida, L., Idiart, M., & Lisman, J. E. (2009). The input–output transformation of the hippocampal granule cells: from grid cells to place fields. *Journal of Neuroscience*, *29*(23), 7504-7512.

Doeller, C. F., Barry, C., & Burgess, N. (2010). Evidence for grid cells in a human memory network. Nature, 463(7281), 657-661. https://doi.org/10.1038/nature08704

Dragoi, G., & Tonegawa, S. (2011). Preplay of future place cell sequences by hippocampal cellular assemblies. *Nature*, *469*(7330), 397-401.

De Cothi, W., Nyberg, N., Griesbauer, E. M., Ghanamé, C., Zisch, F., Lefort, J. M., ... & Spiers, H. J. (2022). Predictive maps in rats and humans for spatial navigation. Current Biology, 32(17), 3676-3689.

Eichenbaum, H., & Lipton, P. A. (2008). Towards a functional organization of the medial temporal lobe memory system: role of the parahippocampal and medial entorhinal cortical areas. *Hippocampus*, *18*(12), 1314-1324.

Epstein, R. A., Patai, E. Z., Julian, J. B., & Spiers, H. J. (2017). The cognitive map in humans: spatial navigation and beyond. *Nature neuroscience*, *20*(11), 1504-1513.

Edvardsen, V., Bicanski, A., & Burgess, N. (2020). Navigating with grid and place cells in cluttered environments. Hippocampus, 30(3), 220-232.

Fyhn, M., Hafting, T., Treves, A., Moser, M. B., & Moser, E. I. (2007). Hippocampal remapping and grid realignment in entorhinal cortex. Nature, 446(7132), 190-194.

Friese, U., Köster, M., Hassler, U., Martens, U., Trujillo-Barreto, N., & Gruber, T. (2013). Successful memory encoding is associated with increased cross-frequency coupling between frontal theta and posterior gamma oscillations in human scalp-recorded EEG. Neuroimage, 66, 642-647.

Fiebelkorn, I. C., Pinsk, M. A., & Kastner, S. (2018). A Dynamic Interplay within the Frontoparietal Network Underlies Rhythmic Spatial Attention. Neuron, 99(4), 842-853 e848. https://doi.org/10.1016/j.neuron.2018.07.038

Fuhs, M. C., & Touretzky, D. S. (2006). A spin glass model of path integration in rat medial entorhinal cortex. Journal of Neuroscience, 26(16), 4266-4276.

Gauthier, I., & Tarr, M. J. (1997). Becoming a "Greeble" expert: exploring mechanisms for face recognition. Vision Res, 37(12), 1673-1682. https://doi.org/10.1016/s0042-6989(96)00286-6

Gallistel, C. R. (2017). Navigation: whence our sense of direction?. *Current Biology*, *27*(3), R108-R110.

Gao, R., Xie, J., Zhu, S. C., & Wu, Y. N. (2018). Learning Grid Cells as Vector Representation of Self-Position Coupled with Matrix Representation of Self-Motion. In International Conference on Learning Representations.

Gerlei, K., Passlack, J., Hawes, I., Vandrey, B., Stevens, H., Papastathopoulos, I., & Nolan, M. F. (2020). Grid cells are modulated by local head direction. Nature communications, 11(1), 4228.

Garcia, A. D., & Buffalo, E. A. (2020). Anatomy and function of the primate entorhinal cortex. *Annual Review of Vision Science*, *6*, 411-432.

Gardner, R. J., Hermansen, E., Pachitariu, M., Burak, Y., Baas, N. A., Dunn, B. A., ... & Moser, E. I. (2022). Toroidal topology of population activity in grid cells. *Nature*, *602*(7895), 123-128.

Hubel, D. H., & Wiesel, T. N. (1959). Receptive fields of single neurones in the cat's striate cortex. J Physiol, 148, 574-591. https://doi.org/10.1113/jphysiol.1959.sp006308

Hubel, D. H., & Wiesel, T. N. (1962). Receptive fields, binocular interaction and functional architecture in the cat's visual cortex. J Physiol, 160, 106-154. https://doi.org/10.1113/jphysiol.1962.sp006837

Hermer, L., & Spelke, E. S. (1994). A geometric process for spatial reorientation in young children. Nature, 370(6484), 57-59.

Hafting, T., Fyhn, M., Molden, S., Moser, M. B., & Moser, E. I. (2005). Microstructure of a spatial map in the entorhinal cortex. Nature, 436(7052), 801-806. https://doi.org/10.1038/nature03721

Hasselmo, M. E. (2009). A model of episodic memory: mental time travel along encoded trajectories using grid cells. Neurobiology of learning and memory, 92(4), 559-573.

Hales, J. B., Schlesiger, M. I., Leutgeb, J. K., Squire, L. R., Leutgeb, S., & Clark, R. E. (2014). Medial entorhinal cortex lesions only partially disrupt hippocampal place cells and hippocampus-dependent place memory. Cell reports, 9(3), 893-901.

Insausti, R., Juottonen, K., Soininen, H., Insausti, A. M., Partanen, K., Vainio, P., Laakso, M. P., & Pitkanen, A. (1998). MR volumetric analysis of the human entorhinal, perirhinal, and temporopolar cortices. AJNR Am J Neuroradiol, 19(4), 659-671. https://www.ncbi.nlm.nih.gov/pubmed/9576651

Iglesias, J. E., Augustinack, J. C., Nguyen, K., Player, C. M., Player, A., Wright, M., Roy, N., Frosch, M. P., McKee, A. C., Wald, L. L., Fischl, B., Van Leemput, K., & Alzheimer's Disease Neuroimaging, I. (2015). A computational atlas of the hippocampal formation using ex vivo, ultra-high resolution MRI: Application to adaptive segmentation of in vivo MRI. Neuroimage, 115, 117-137. https://doi.org/10.1016/j.neuroimage.2015.04.042

Jenkinson, M., & Smith, S. (2001). A global optimisation method for robust affine registration of brain images. Med Image Anal, 5(2), 143-156. https://doi.org/10.1016/s1361-8415(01)00036-6

Johnson, A., Seeland, K., & Redish, A. D. (2005). Reconstruction of the postsubiculum head direction signal from neural ensembles. Hippocampus, 15(1), 86-96.

Jeffery, K. J. (2007). Integration of the sensory inputs to place cells: what, where, why, and how?. *Hippocampus*, *17*(9), 775-785.

Julian, J. B., Keinath, A. T., Muzzio, I. A., & Epstein, R. A. (2015). Place recognition and heading retrieval are mediated by dissociable cognitive systems in mice. Proceedings of the National Academy of Sciences, 112(20), 6503-6508.

Jeffery, K. J., Page, H. J., & Stringer, S. M. (2016). Optimal cue combination and landmark-stability learning in the head direction system. The Journal *of physiology*, *594*(22), 6527-6534.

Julian, J. B., Keinath, A. T., Marchette, S. A., & Epstein, R. A. (2018). The neurocognitive basis of spatial reorientation. *Current Biology*, *28*(17), R1059-R1073.

Krupic, J., Burgess, N., & O'Keefe, J. (2012). Neural representations of location composed of spatially periodic bands. Science, 337(6096), 853-857. https://doi.org/10.1126/science.1222403

Killian, N. J., Jutras, M. J., & Buffalo, E. A. (2012). A map of visual space in the primate entorhinal cortex. Nature, 491(7426), 761-764. https://doi.org/10.1038/nature11587

Krupic, J., Bauza, M., Burton, S., Barry, C., & O'Keefe, J. (2015). Grid cell symmetry is shaped by environmental geometry. *Nature*, *518*(7538), 232-235.

Keinath, A. T., Julian, J. B., Epstein, R. A., & Muzzio, I. A. (2017). Environmental geometry aligns the hippocampal map during spatial reorientation. *Current Biology*, *27*(3), 309-317.

Kang, L., & Balasubramanian, V. (2019). A geometric attractor mechanism for self-organization of entorhinal grid modules. Elife, 8, e46687.

Landau, A. N., & Fries, P. (2012). Attention samples stimuli rhythmically. Curr Biol, 22(11), 1000-1004. https://doi.org/10.1016/j.cub.2012.03.054

Leutgeb, S., Ragozzino, K. E., & Mizumori, S. J. (2000). Convergence of head direction and place information in the CA1 region of hippocampus. Neuroscience, 100(1), 11-19.

Lisman, J., Buzsáki, G., Eichenbaum, H., Nadel, L., Ranganath, C., & Redish, A. D. (2017). Viewpoints: how the hippocampus contributes to memory, navigation and cognition. Nature neuroscience, 20(11), 1434-1447.

McNaughton, B. L., Barnes, C. A., & O'Keefe, J. J. E. B. R. (1983). The contributions of position, direction, and velocity to single unit activity in the hippocampus of freely-moving rats. *Experimental brain research*, *52*, 41-49.

Muller, R. U., Bostock, E., Taube, J. S., & Kubie, J. L. (1994). On the directional firing properties of hippocampal place cells. *Journal of Neuroscience*, *14*(12), 7235-7251.

Montaldi, D., & Mayes, A. R. (2010). The role of recollection and familiarity in the functional differentiation of the medial temporal lobes. *Hippocampus*, *20*(11), 1291-1314.

Maris, E., van Vugt, M., & Kahana, M. (2011). Spatially distributed patterns of oscillatory coupling between high-frequency amplitudes and low-frequency phases in human iEEG. Neuroimage, 54(2), 836-850.

Mullally, S. L., & Maguire, E. A. (2014). Memory, imagination, and predicting the future: A common brain mechanism?. The Neuroscientist, 20(3), 220-234.

Meister, M. L., & Buffalo, E. A. (2016). Getting directions from the hippocampus: The neural connection between looking and memory. Neurobiology of learning and memory, 134, 135-144.

Munn, R. G., Mallory, C. S., Hardcastle, K., Chetkovich, D. M., & Giocomo, L. M. (2020). Entorhinal velocity signals reflect environmental geometry. Nature neuroscience, 23(2), 239-251.

Muhle-Karbe, P. S., Sheahan, H., Pezzulo, G., Spiers, H. J., Chien, S., Schuck, N. W., & Summerfield, C. (2023). Goal-seeking compresses neural codes for space in the human hippocampus and orbitofrontal cortex. Neuron.

Morris, G., & Derdikman, D. (2023). The chicken and egg problem of grid cells and place cells. Trends in Cognitive Sciences.

Naber, P. A., Lopes da Silva, F. H., & Witter, M. P. (2001). Reciprocal connections between the entorhinal cortex and hippocampal fields CA1 and the subiculum are in register with the projections from CA1 to the subiculum. Hippocampus, 11(2), 99-104.

Nichols, T. E., & Holmes, A. P. (2002). Nonparametric permutation tests for functional neuroimaging: a primer with examples. Hum Brain Mapp, 15(1), 1-25. https://doi.org/10.1002/hbm.1058

Nau, M., Navarro Schroder, T., Bellmund, J. L. S., & Doeller, C. F. (2018). Hexadirectional coding of visual space in human entorhinal cortex. Nat Neurosci, 21(2), 188-190. https://doi.org/10.1038/s41593-017-0050-8

Nyberg, N., Duvelle, É., Barry, C., & Spiers, H. J. (2022). Spatial goal coding in the hippocampal formation. Neuron.

O'Keefe, J., & Dostrovsky, J. (1971). The hippocampus as a spatial map: preliminary evidence from unit activity in the freely-moving rat. Brain research. https://doi.org/10.1016/0006-8993(71)90358-1

O'keefe, J., & Burgess, N. (2005). Dual phase and rate coding in hippocampal place cells: theoretical significance and relationship to entorhinal grid cells. Hippocampus, 15(7), 853-866.

Ormond, J., & O'Keefe, J. (2022). Hippocampal place cells have goal-oriented vector fields during navigation. Nature, 607(7920), 741-746.

Park, S. A., Miller, D. S., Nili, H., Ranganath, C., & Boorman, E. D. (2020). Map making: constructing, combining, and inferring on abstract cognitive maps. *Neuron*, *107*(6), 1226-1238.

Pfeiffer, B. E. (2020). The content of hippocampal “replay”. Hippocampus, 30(1), 6-18.

Poulter, S., Lee, S. A., Dachtler, J., Wills, T. J., & Lever, C. (2021). Vector trace cells in the subiculum of the hippocampal formation. Nature neuroscience, 24(2), 266-275.

Rubin, A., Yartsev, M. M., & Ulanovsky, N. (2014). Encoding of head direction by hippocampal place cells in bats. Journal of Neuroscience, 34(3), 1067-1080.

Raithel, C. U., Miller, A. J., Epstein, R. A., Kahnt, T., & Gottfried, J. A. (2023). Recruitment of grid-like responses in human entorhinal and piriform cortices by odor landmark-based navigation. Current Biology, 33(17), 3561-3570.

Samsonovich, A., & McNaughton, B. L. (1997). Path integration and cognitive mapping in a continuous attractor neural network model. J Neurosci, 17(15), 5900-5920. https://www.ncbi.nlm.nih.gov/pubmed/9221787

Solstad, T., Moser, E. I., & Einevoll, G. T. (2006). From grid cells to place cells: a mathematical model. Hippocampus, 16(12), 1026-1031. https://doi.org/10.1002/hipo.20244

Sargolini, F., Fyhn, M., Hafting, T., McNaughton, B. L., Witter, M. P., Moser, M. B., & Moser, E. I. (2006). Conjunctive representation of position, direction, and velocity in entorhinal cortex. Science, 312(5774), 758-762.

Stam, C. J., Nolte, G., & Daffertshofer, A. (2007). Phase lag index: assessment of functional connectivity from multi channel EEG and MEG with diminished bias from common sources. Human brain mapping, 28(11), 1178-1193.

Stemmler, M., Mathis, A., & Herz, A. V. (2015). Connecting multiple spatial scales to decode the population activity of grid cells. Sci Adv, 1(11), e1500816. https://doi.org/10.1126/science.1500816

Schlichting, M. L., Mumford, J. A., & Preston, A. R. (2015). Learning-related representational changes reveal dissociable integration and separation signatures in the hippocampus and prefrontal cortex. Nat Commun, 6, 8151. https://doi.org/10.1038/ncomms9151

Stensola, T., Stensola, H., Moser, M. B., & Moser, E. I. (2015). Shearing-induced asymmetry in entorhinal grid cells. *Nature*, *518*(7538), 207-212.

Sarel, A., Finkelstein, A., Las, L., & Ulanovsky, N. (2017). Vectorial representation of spatial goals in the hippocampus of bats. *Science*, *355*(6321), 176-180.

Sun, Y., Jin, S., Lin, X., Chen, L., Qiao, X., Jiang, L., ... & Xu, X. (2019). CA1-projecting subiculum neurons facilitate object–place learning. Nature neuroscience, 22(11), 1857-1870.

Tolman, E. C. (1948). Cognitive maps in rats and men. Psychol Rev, 55(4), 189-208. https://doi.org/10.1037/h0061626

Taube, J. S., Muller, R. U., & Ranck, J. B. (1990). Head-direction cells recorded from the postsubiculum in freely moving rats. I. Description and quantitative analysis. Journal of Neuroscience, 10(2), 420-435.

Taube, J. S. (2007). The head direction signal: origins and sensory-motor integration. Annu. Rev. Neurosci., 30, 181-207.

Tsao, A., Moser, M. B., & Moser, E. I. (2013). Traces of experience in the lateral entorhinal cortex. Current biology, 23(5), 399-405.

Toledo, S., Shohami, D., Schiffner, I., Lourie, E., Orchan, Y., Bartan, Y., & Nathan, R. (2020). Cognitive map–based navigation in wild bats revealed by a new high-throughput tracking system. Science, 369(6500), 188-193.

Towers, Mark, Terry, Jordan K, Kwiatkowski, Ariel, Balis, John U., Cola, Gianluca, Deleu, Tristan, Goulão, Manuel, Kallinteris, Andreas, KG, Arjun, Krimmel, Markus, Perez-Vicente, Rodrigo, Pierré, Andrea, Schulhoff, Sander, Tai, Jun Jet, Tan, Andrew Jin Shen, & Younis, Omar G. (2023). Gymnasium (v0.29.0). Zenodo. https://doi.org/10.5281/zenodo.8148697

van Groen, T., Miettinen, P., & Kadish, I. (2003). The entorhinal cortex of the mouse: organization of the projection to the hippocampal formation. Hippocampus, 13(1), 133-149. https://doi.org/10.1002/hipo.10037

VanRullen, R., & Kanai, R. (2021). Deep learning and the Global Workspace Theory. Trends Neurosci, 44(9), 692-704. https://doi.org/10.1016/j.tins.2021.04.005

Witter, M. P., & Amaral, D. G. (1991). Entorhinal cortex of the monkey: V. Projections to the dentate gyrus, hippocampus, and subicular complex. J Comp Neurol, 307(3), 437-459. https://doi.org/10.1002/cne.903070308

Woolrich, M. W., Ripley, B. D., Brady, M., & Smith, S. M. (2001). Temporal autocorrelation in univariate linear modeling of FMRI data. Neuroimage, 14(6), 1370-1386. https://doi.org/10.1006/nimg.2001.0931

Wang, R. F., & Spelke, E. S. (2002). Human spatial representation: Insights from animals. *Trends in cognitive sciences*, *6*(9), 376-382.

Woolrich, M. W., Behrens, T. E., & Smith, S. M. (2004). Constrained linear basis sets for HRF modelling using Variational Bayes. Neuroimage, 21(4), 1748-1761. https://doi.org/10.1016/j.neuroimage.2003.12.024

Winter, S. S., & Taube, J. S. (2014). Head direction cells: from generation to integration. In Space, time and memory in the hippocampal formation (pp. 83-106). Vienna: Springer Vienna.

Welday, A. C., Shlifer, I. G., Bloom, M. L., Zhang, K., & Blair, H. T. (2011). Cosine directional tuning of theta cell burst frequencies: evidence for spatial coding by oscillatory interference. *Journal of Neuroscience*, *31*(45), 16157-16176.

Wilson, D. I., Langston, R. F., Schlesiger, M. I., Wagner, M., Watanabe, S., & Ainge, J. A. (2013). Lateral entorhinal cortex is critical for novel object-context recognition. *Hippocampus*, *23*(5), 352-366.

Whittington, J. C., Muller, T. H., Mark, S., Chen, G., Barry, C., Burgess, N., & Behrens, T. E. (2020). The Tolman-Eichenbaum machine: unifying space and relational memory through generalization in the hippocampal formation. *Cell*, *183*(5), 1249-1263.

Whittington, J. C., McCaffary, D., Bakermans, J. J., & Behrens, T. E. (2022). How to build a cognitive map. *Nature neuroscience*, *25*(10), 1257-1272.

Wagner, I. C., Graichen, L. P., Todorova, B., Lüttig, A., Omer, D. B., Stangl, M., & Lamm, C. (2023). Entorhinal grid-like codes and time-locked network dynamics track others navigating through space. Nature Communications, 14(1), 231.

Zhang, B., Ma, L., & Liu, J. (2023). Experience replay facilitates the formation of the hexagonal pattern of grid cells. bioRxiv, 2023-02.

Methods

Participants

Two groups of right-handed university students with normal or corrected-to-normal vision were recruited. The first group, which served as the experimental group, was 10 students from Peking University, and the second group contained ten students from Tsinghua University for replication purpose. Participants' age and sex were balanced between groups (experimental group: mean age = 22.10 [SD = 2.23], 5 females, 5 males; replication group: mean age = 23.9 [SD = 3.51], 5 females, 5 males). All participants had no history of psychiatric or neurological disorders and gave their written informed consent prior to the experiment, which was approved by the Research Ethics Committee of both universities.

Experimental design

Artificial object space. The greebles (Gauthier and Tarr, 1997) were created by 3ds Max (Autodesk, version 2022, http://www.autodesk.com) and the MAXScript codes from an open-source repository (TarrLab stimulus datasets, http://www.tarrlab.org/). The identity of individual greeble was determined by the lengths of its two components, named as "Loogit" and "Vacso", These names were arbitrary and had no relation to the object matching task (Fig.1a). We created 2025 greebles in total, each of which was equipped with a unique combination of Loogit's and Vacso's length. In this way, a 45-by-45 object space was constructed, with y-axis denoting Loogit's length and x-axis denoting Vacso's length (Fig. 1c). Therefore, in this 2-D artificial object space, each greeble represented a location. The greeble in the center of the space had equal length of Loogit and Vacso (i.e., the prototype highlighted by blue dot in Fig.1c), which served as the target of the task. The ratio of a greeble components' length over that of the prototype ranged from 0.12 to 1.88 with a step size of 0.04, which offered a smooth morphing experience when participants adjusted the length of greeble components.

Experimental procedure. In a trial of the object matching task, a greeble variant that was pseudo-randomly selected from greeble variants on the ring near the boundary of the space (orange dots in Fig.1c & d) was presented in the center of the screen after a 2.0-s fixation screen (Fig.1b). Participants adjusted the lengths of the variant to match the prototype as quickly as possible by pressing buttons. There were four buttons, two of which were used to either stretching or shrinking

the greeble components. Participants either pressed the return key to end the trial (self-pace in behavioral training) or waited the time limit to run out (the fixed time limit of 10 secs in fMRI scan) when they subjectively adjusted the variant completely matching the prototype. To ensure paths from variants to the prototype covered most of locations in the space, 24 variants were randomly selected from each 30° bin of the ring with angular precision of 1°. This procedure made up a total of 288 variants evenly selected in the ring. The accuracy of a trial was indexed by the distance between prototype's location and the location where the participant stopped. To encourage the participants to perform the task as accurately as possible, participants were informed that the amount of their monetary compensation increased exponentially with their performance. The task was programmed by Python (version 3.9) and Pygame (a library designed for writing video games, version 2.0, https://www.pygame.org/).

The task was conducted twice in two consecutive days, one for behavioral training and the other for fMRI scan. On day 1, the participants adjusted the length of variant's parts to match the prototype in a self-paced fashion. There were 8 sessions with 36 trials each, these 288 trials took about 1 hour. The first 7 sessions provided feedback at the end of trials (e.g., "Loogit: 5 percent longer than the target") and the 8th session had no feedback for measuring behavioral performance. Before the training, participants learned the prototype by watching it on the screen, and then performed at least 10 trials with feedback as practice. On day 2, the experiment procedure was identical to that of day 1, except that (1) the self-pace was replaced with a 10-s time limit for each trial with a timer presented on top of screen (Fig.1b), (2) no feedback was provided for all the trials, and (3) participants finished the experiment in fMRI scanner. After the fMRI scan, participants were debriefed, and none of them was aware of the existence of object space or the analogy of the adjustment of spatial components in the experiment. The behavioral performance of participants that fluctuates as a function of conceptual directions was defined by $0.04 \times T + E$, where T represents the path length defined by movement steps, which was scaled into the distance of object space by a constant parameter 0.04, E denotes the error quantified by the distance between the goal-location and the location participants stopped in object space.

fMRI data acquisition

1060 Imaging data were collected using a 3T Siemens Prisma scanner equipped with a 64- and 20-
1061 channel receiver head coil for the experimental group and replication group at PKU and Tsinghua
1062 Imaging Center, respectively. Functional data were acquired with a Multi-band Echo Planer
1063 imaging (EPI) sequence (TR = 2000 ms, TE = 30 ms, matrix size: 112 × 112 x 62, flip angle: 90°,
1064 resolution: 2 × 2 × 2.3 mm^3, number of slices: 62, slice thickness: 2 mm, gap = 0.3 mm, slice
1065 orientation: transversal). A high-resolution T1-weighted three-dimensional anatomical data set
1066 was collected for registration (MPRAGE, TR = 2530 ms, TE = 2.98 ms, matrix size: 448 x 512 x
1067 192, flip angle: 7°, resolution: 0.5 × 0.5 × 1 mm3, number of slices: 192, slice thickness: 1 mm,
1068 slice orientation: sagittal). In the experimental group, stimuli were presented through a Sinorad
1069 LCD projector (Shenzhen Sinorad Medical Electronics) onto a 33-inch rear-projection screen. In
1070 the replication group, the stimuli were presented using a visual/audio stimulation system
1071 (Shenzhen Sinorad SA-9939) with a customized-design (Shenzhen Sinorad Medical Electronics
1072 Co., Ltd) MRI compatible 40" LED liquid crystal display. The resolution of screens was 1024 x
1073 768, and the participants viewed the stimuli with an angled mirror mounted on the head coil.
1074
1075 **fMRI data preprocessing**
1076 The BOLD signal series of each scan session was preprocessed independently using FSL FEAT
1077 toolbox (FMRIB's Software Library, version 6.0, https://fsl.fmrib.ox.ac.uk/fsl/fslwiki; Woolrich
1078 et al. 2001; Woolrich et al. 2004). For each session, the signal series were corrected for motion
1079 artifacts, slice time acquisition differences, geometrical distortion using fieldmaps, and were high-
1080 pass filtered at 100 s. Spatial smoothing was further applied using a 5 mm FWHM Gaussian kernel.
1081 For group-level statistics, the signal series of each session were registered to participant's high-
1082 resolution anatomical image and were then normalized to a standard image (MNI152) using FSL
1083 FLIRT (Jenkinson and Smith, 2001). This procedure also resampled the functional voxels into a 2
1084 x 2 x 2 mm resolution.
1085
1086 **Sinusoid analysis**
1087 To test whether the grid cell activity was present during the object matching task, we first
1088 computed the grid orientation in the ERC for each participant using one half of the data (odd-
1089 numbered sessions). Second, we examined the grid pattern that was modulated by participants'
1090 path directions ranging from 0° to 360° in the object space after controlling for the effect of grid

orientation (Doeller et al., 2010; Constantinescu et al., 2016; Bao et al., 2019; Wagner et al., 2023; Raithel et al., 2023). Specifically, a GLM was created for each session to model the BOLD signal series convolved with FSL Double-Gamma hemodynamic response function in the ERC with two parametric modulators: sin(6θ) and cos(6θ), where θ represents the path directions in the object space. The factor 6 means the 6-folded neural activity, which is rotational symmetric and aligned with path directions. The factor 5 and 7 were used as controls, which misaligned with the primary axes of grid cells. Those estimated parameters β_{sine} and β_{cosine} were subsequently used to compute the grid orientation φ, ranged from 0° to 59°, in each voxel and each participant, where $\varphi = [\arctan(\frac{\beta_{sine}}{\beta_{cosine}})]/6$. The grid orientation Φ for each participant was derived by averaging the φ map across the odd-numbered sessions and voxels in the ERC. Once the 6-fold neural activity in the ERC was identified, a second GLM was fitted to model the BOLD signal series from the other half of the data (even-numbered sessions), which was specified by a cosine parametric modulator: cos(6[θ - Φ]). The activity map of the ERC was derived by averaging the parametric map of this cosine modulator across the even-numbered sessions, which was further converted to z-score map before submitting to second-level analysis (Schlichting et al., 2015).

Spectral analysis of MRI BOLD signals

To examine the spatial periodicity of BOLD signal series within the HPC, we created a GLM to extract the activity maps corresponding to movement directions in the object space. Then, voxel-based spectral analyses were performed to identify spatially periodic activity within the MTL. Specifically, the movement directions, which were represented by the paths from greeble variants to prototype, were first down-sampled into bins with 15° each (e.g., the movement directions within -7.5° to 7.5°was label as 0° and the movement directions within 337.5° to 352.5°was label as 345°). This procedure resulted in a vector of 24 resampled movement directions (i.e., the number of bins), which was sufficient samples for spectral analysis (De Valois et al., 1982) and was used to examine the spatial periodicity of the HPC with a spatial frequency range from 0- to 11-fold. Next, the BOLD signal series of each voxel was modelled by a GLM with the 24 directional bins specified as parametric modulators, producing a vector of 24 direction-dependent activity maps for each participant, which were sorted in ascending order (i.e., from 0° to 360°). The direction-based activity vector was detrended before spectral analysis was performed using the Fast Discrete Fourier Transform (FFT) (the stats package of R platform, version 4.0, https://www.r-project.org/;

Landau and Fries, 2012). In this way, the BOLD signal series were converted into frequency domain from spatial domain. Spectral magnitude was derived by computing the absolute values of the complex FFT output. This procedure generated a brain map of spectrum magnitude for each spatial fold. The 95th percentile of pseudo t-statistic distribution (i.e., mean spectral magnitude divided by SE across human participants) was computed as the initial threshold in second-level analysis before correction for multiple comparisons.

Spectral analysis of human behavior

As to human behavior, we first defined their navigation efficiency for any movement direction using a composite score, which was derived by the linear summation of the path length for the direction and the error size between participant's ending-location and the goal-location. A high efficiency was characterized by shorter travel lengths and smaller error size. This procedure generated a vector of navigation efficiency as a function of movement directions for each participant. The behavioral efficiency vector was further down-sampled using 10° bin, resulting into 36 sample points. Second, the movement directions of human participants were constrained by four buttons (i.e., move to "East", "South", "West", and "North"), which brings a confounding factor in path length among movement directions (e.g., the "East" path would be shorter than the "Southeast" path). To remove this confounding effect, we computed the optimized path length for each starting-location, which was subtracted by the path length recorded from participants. This operation allows us to capture the pure behavioral bias in movement direction induced by hippocampal periodicity. Third, the spectral and second-level analysis of behavioral efficiency was identical to the procedure applied in MRI BOLD signal series.

Anatomical masks

We manually delineated the bilateral ERC for ROI analyses on the MNI T1 brain with 2 mm resolution packaged by FSL using established protocols (Insausti et al. 1998), as well as a delineating software ITK-SNAP (Version 3.8, www.itksnap.org). The masks of HPC subfields were derived by an automated segmentation tool packaged by Freesurfer (Version 7.1, https://surfer.nmr.mgh.harvard.edu/; Iglesias et al., 2015), which segments the CA1 and CA2/3 area from hippocampal formation and further divides the mask into head and body parts. All masks were resampled to 2 mm resolution and aligned in standard MNI space.

1153

1154 **The "E-H PhaseSync" model**

1155 The model, implemented using Python (version 3.9), is hypothesized to elucidate the mechanism
1156 of the 3-fold periodicity formation in the HPC. The agent is programmed to perform path
1157 integration on a 45-by-45-pixel space, where each location (1 out of 2025 pixels) is denoted by
1158 coordinate vector $r = (x, y)$. The goal-location is located in space center $r = (22,22)$. The model
1159 hypothesizes that hippocampal directional representation relies on the projections of entorhinal
1160 grid cells. Specifically, grid cell population activated by mental imagination projects conjunctive
1161 grid codes to downstream areas (Witter and Amaral, 1991; van Groen et al., 2003; Fyhn et al.,
1162 2007; Hasselmo, 2009; Buckner, 2010; Hales et al., 2014; Mullally and Maguire, 2014; Garcia and
1163 Buffalo, 2020), where VTCs in the subiculum (Tsao et al., 2013; Bicanski and Burgess, 2018;
1164 Bicanski and Burgess, 2020; Poulter et al., 2021), inherit the grid codes and form the periodic
1165 scaffold to represent spatial orientations, then hippocampal place cells further inherit the periodic
1166 scaffold to embed path directions using multi-scale encoding. Finally, the vector field is generated
1167 by the direction map with distance binding, which conforms with winner-take-all dynamics
1168 (Bicanski and Burgess, 2019).

1169

1170 *Simulation of Entorhinal Grid cell*. Grid cells are generated using the cosine grating model
1171 (O'keefe and Burgess, 2005; Burgess et al., 2007; Blair et al., 2007; Bush and Schmidt-Hieber,
1172 2018). For single grid cell, the spatial code G at spatial location $r_{(x,y)}$ is generated by summing
1173 three cosine gratings under the spatial phase $c_{(x,y)}$(Equation 6). The cosine gratings are oriented
1174 by the rotation vector k with 60° apart from one another. The parameter A denotes the amplitude
1175 of cosine gratings. For simulating multi-scale encoding, four spatial scales of grid cells (i.e.,
1176 denoted by grid module Ω) are generated for each location $r_{(x,y)}$. The scale-ratio of Ω is defined at
1177 approximately 1.4 (Kang and Balasubramanian, 2019; Killian et al., 2012; Stemmler et al., 2015).
1178 A total of 2025 grid cells are generated for each Ω. Constant grid orientation is used for all grid
1179 cells while grid phase varied.

1180 $$G_r = \sum_{i=1}^{3} A\cos(\omega_i(k_{i,x}(r_x - c_x) + k_{i,y}(r_y - c_y))) \quad (6)$$

1181 *Simulation of subiculum vector trace cell.* Vector trace cells (VTCs) are simulated using the
1182 conjunctive representation of grid cells activated by path planning (Fig.3a, Buckner, 2010;
1183 Mullally and Maguire, 2014; Lisman et al., 2017; Whittington et al., 2022). For single VTC, the

trace field V is defined as exp $(\sum_i^k G_i)$, where G denotes the grid code, i and k denote the starting- and goal-location, respectively. Previous studies found that VTC encodes the sequential locations of objects (Tsao et al., 2013; Bicanski and Burgess, 2018; Bicanski and Burgess, 2020; Poulter et al., 2021). Correspondingly, VTCs are assumed to encode sequential locations of self-body in the model during path planning. Given the symmetry of object space, the vector trace field V is symmetrical for the path direction ϕ and the direction $\phi + 180^\circ$ (Fig.3b), naturally reflecting the spatial orientation ψ of object space. In this case, the object space is tessellated by VTC population in the subiculum, which encodes the spatial orientations ranged from 0 to π.

$$\delta_r = \begin{cases} \left|\Psi_{max,r} - (\emptyset_r \; mod \; \pi)\right|, & if \; \Psi_{max,r} > \Psi_{mean,r} + 2\sigma \\ 1 & otherwise \end{cases} \tag{7}$$

The activation strength δ of each VTC is indexed by how closely the encoded spatial orientation ψ aligns to the path direction ϕ (Equation 7), a process similar to the determination of head directions (Taube et al., 1990; Johnson et al., 2005; Taube, 2007; Winter and Taube, 2014). Specifically, we first compute Ψ for a given vector trace field V (Equation 2), which represents a vector of orientation selectivity. ψ was then identified by the maxima of Ψ using the find_peaks function (Scipy, version 1.9.3), if the Ψ_{max} exceeds the threshold of $2\times\sigma$ (i.e., standard deviation) from the mean (Equation 7). Otherwise, a constant value of one was assigned to the VTC cell. Path direction ϕ is defined by arctan $(\frac{r'_y}{r'_x})$, which is ranged from 0° to 360°. r'_x and r'_y denote the relative distance between self- and goal-location Next, ψ is compared with path direction ϕ, the angle difference is normalized into 0 to 1 to represent the activity strength of VTC cell (Equation 8).

$$\delta_{normalized,r} = 1 - \frac{\delta_r - \delta_{min}}{\delta_{max} - \delta_{min}} \tag{8}$$

Simulation of Hippocampal vector field. Vector field C is generated by integrating the movement direction map $C_{Direction}$ and the distance map $C_{Location}$ (Equation 5). Both of which denote a two-dimensional hippocampal activity matrix averaged across Ω. Specifically, $C_{Direction}$ is computed by a cosine function with the frequency c_δ and phase ε_δ inherited from the δ map (Equation 4), which receives path direction ϕ as input and outputs movement direction θ for each location r (Equation 4). $C_{Location}$, which is insensitive to path directions but encodes the distance between self- and goal-location, is defined by a Q-value map over the two-dimensional space trained from a standard RL model using Gymnasium library (OpenAI, version=0.29; Towers et al., 2023).

During simulation, a total of 156 locations, forming a ring-shaped pattern near the boundary of space, serve as the starting-locations. In each movement step, a vector of place cell activity from the locations surrounding self-location is extracted from C, agent transitions to next location by looking for the location with the strongest activity in the vector. The step size is adapted to a stepwise approach. The step size of 1 pixel is initialized, and the size is increased by 1 pixel if no stronger activity is found from the surrounding locations. The coordinate sequences between the starting- and the goal-location are recorded during the simulation. The path length is computed by the sum of the distances of every location-pairs. The vector of path lengths across path directions are then sorted with ascending order before submitting to spectrum analysis.

Statistical analysis

The 6-fold and 3-fold neural periodicity were examined by cluster-based permutation using FSL randomise package (version 2.9, http://fsl.fmrib.ox.ac.uk/fsl/fslwiki/Randomise), where an initial threshold of $p < 0.01$ was used to derive the uncorrected clusters. If no clusters were revealed, a liberal threshold of $p < 0.05$ was used. The reliability of the uncorrected clusters was further tested using a non-parametric statistical inference that does not make assumptions about the distribution of the data (Nichols and Holmes 2002). Specifically, 5,000 random sign-flips were performed on the beta or FFT magnitude images. The clusters with size higher than 95% of the maximal suprathreshold clusters from permutation distribution were reported. The periodicity of behavioral performance recorded from the "E-H PhaseSync" model and human participants was examined using FFT, where the initial threshold of each frequency was derived from the 95% percentile of shuffled magnitude distribution, the threshold corrected for multiple comparison was selected by the maximum of the initial thresholds across frequencies. The coherence between the BOLD signal series of the ERC and the HPC was examined using the amplitude-phase coupling analysis (Canolty et al., 2006), where no band-passed filter was applied. The coherence between the BOLD signal series of the HPC and human behavioral efficiency was examined using the phase-lag index (Stam et al., 2007), where the signal series of both human behavior and brain activity were band-passed filtered using EEGLAB (Version 2023, https://eeglab.org/). The robustness of coherence was evaluated by permutation test with 5000 shuffling applied on the path directions. The

coherence that higher than the top 5% of shuffled distribution was considered to be significant. All the t-tests used in the present study were two-tailed.

Supplemental Material

"The spatial periodic computation of hippocampus-entorhinal circuit in navigation"

Bo Zhang and Jia Liu

Figure S1. Behavioral results of human participants from experimental and replication group. The error was defined as the distance between the prototype location and the location where participants stopped. On day 1, task errors decreased as a function of experimental sessions, resulting a significantly negative slope for both groups of participants (experimental group: $t(9) = -3.90$, $p = 0.003$; replication group: $t(9) = -2.82$, $p = 0.019$). No significant learning effect was found on day 2 (experimental group: $t(9) = -0.22$, $p = 0.834$; replication group: $t(9) = -0.10$, $p = 0.922$). This design ruled out the possibility of learning effect in examining the spatial periodicity of the HPC. Error bars indicate SEM.

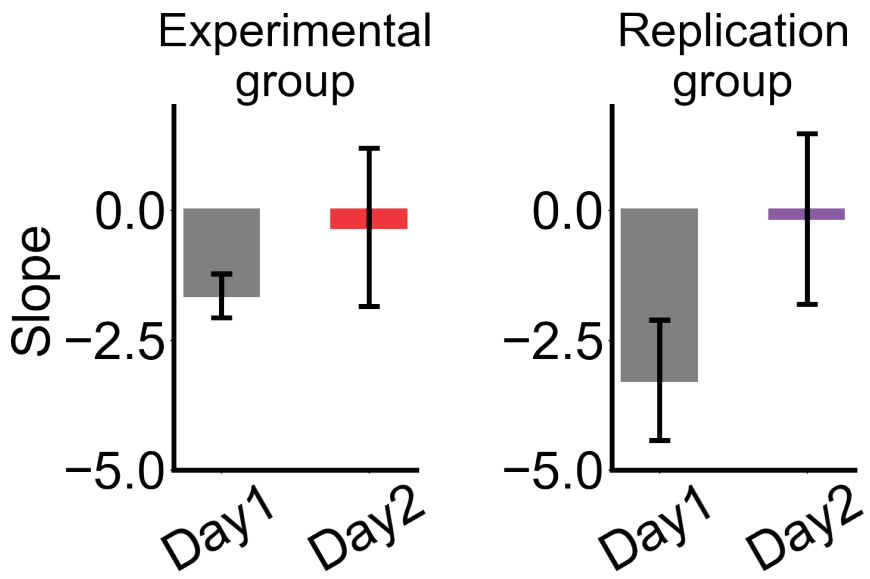

Figure S2. Paths of human participants recorded during MRI scanning. The orange dots denote the starting-locations while the red/purple dots indicate the ending-locations for the experimental (red) and replication (purple) group.

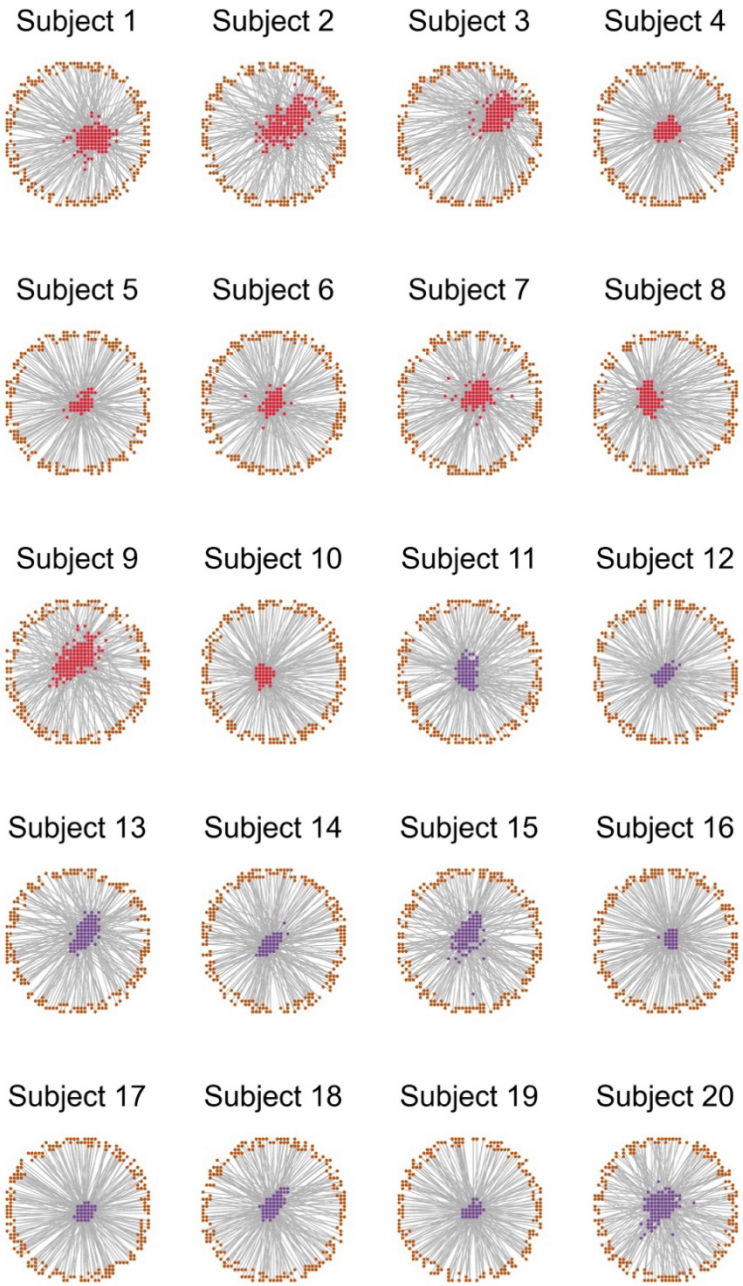

Figure S3. Distribution of grid orientations in the ERC of the experimental (red) and replication (purple) group. The uniformity of grid orientations, which was computed for each voxel, was tested by Rayleigh test. All participants showed significantly clustered grid orientations ($p < 0.05$, Bonferroni corrected). The length of bars indicates the number of voxels and the black line denotes the mean of hexagonal orientations.

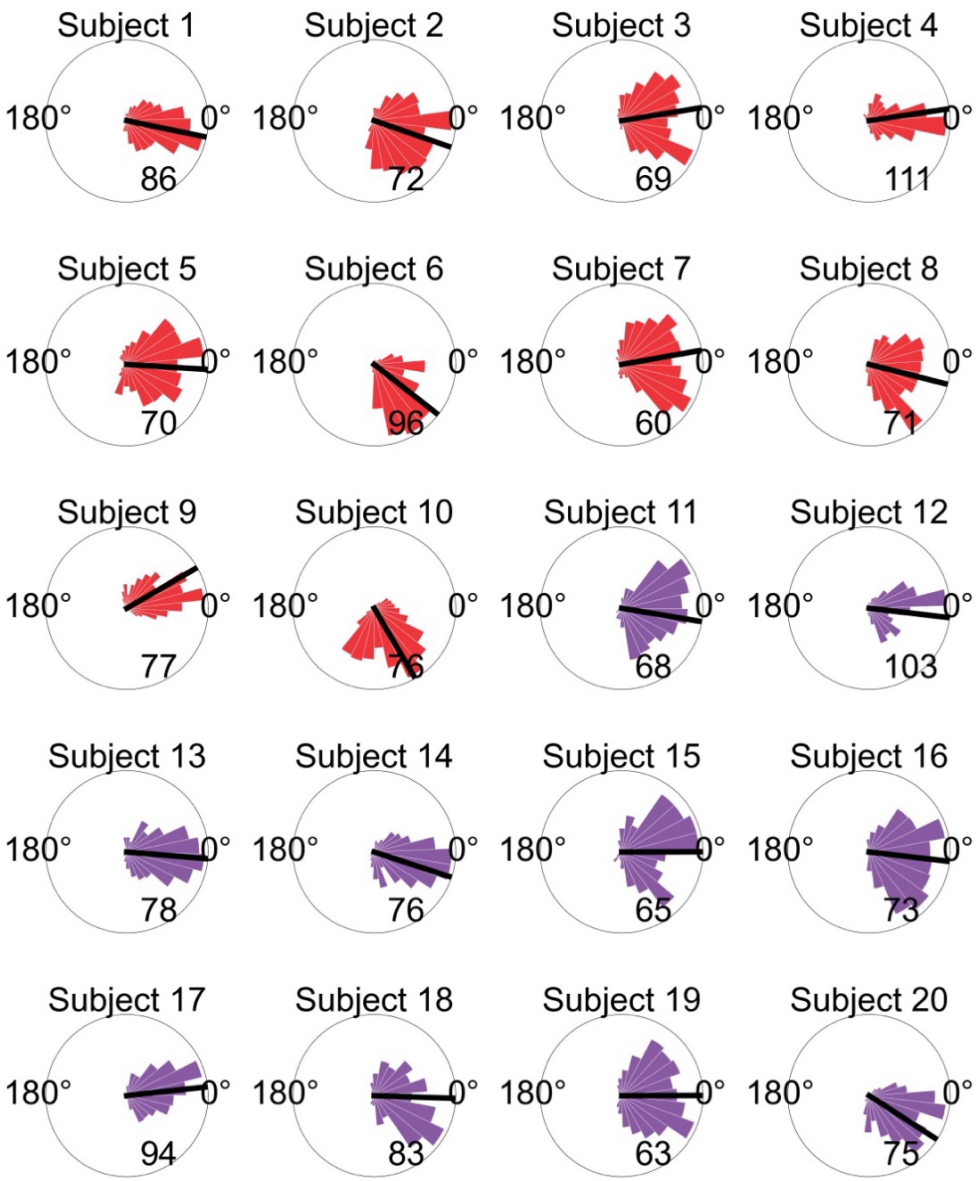

Figure S4. 3-fold modulation of the HPC examined using 10° and 20° bin. The significant clusters were robustly revealed in the right HPC (initial threshold on pseudo t-value: $p < 0.05$; SVC for multiple comparison: $p < 0.05$). The x & y value denote MNI coordinate.

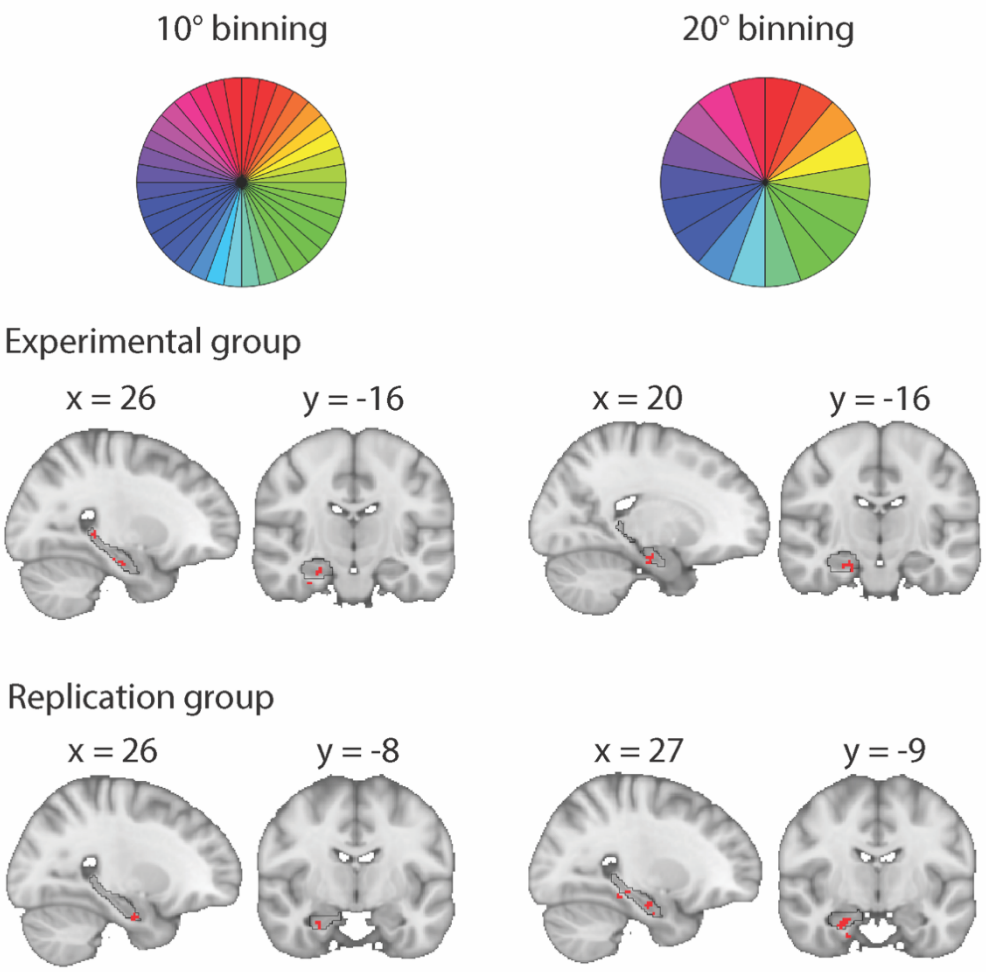

Figure S5. Spatial periodicity of the ERC and the HPC observed in the replication group. The 6- and 3-fold modulation, detected by sinusoid and spectral analysis, was shown in the right ERC and the right HPC, respectively (initial threshold: $p < 0.01$; SVC for multiple comparisons: $p < 0.05$). Error bar denotes SEM.

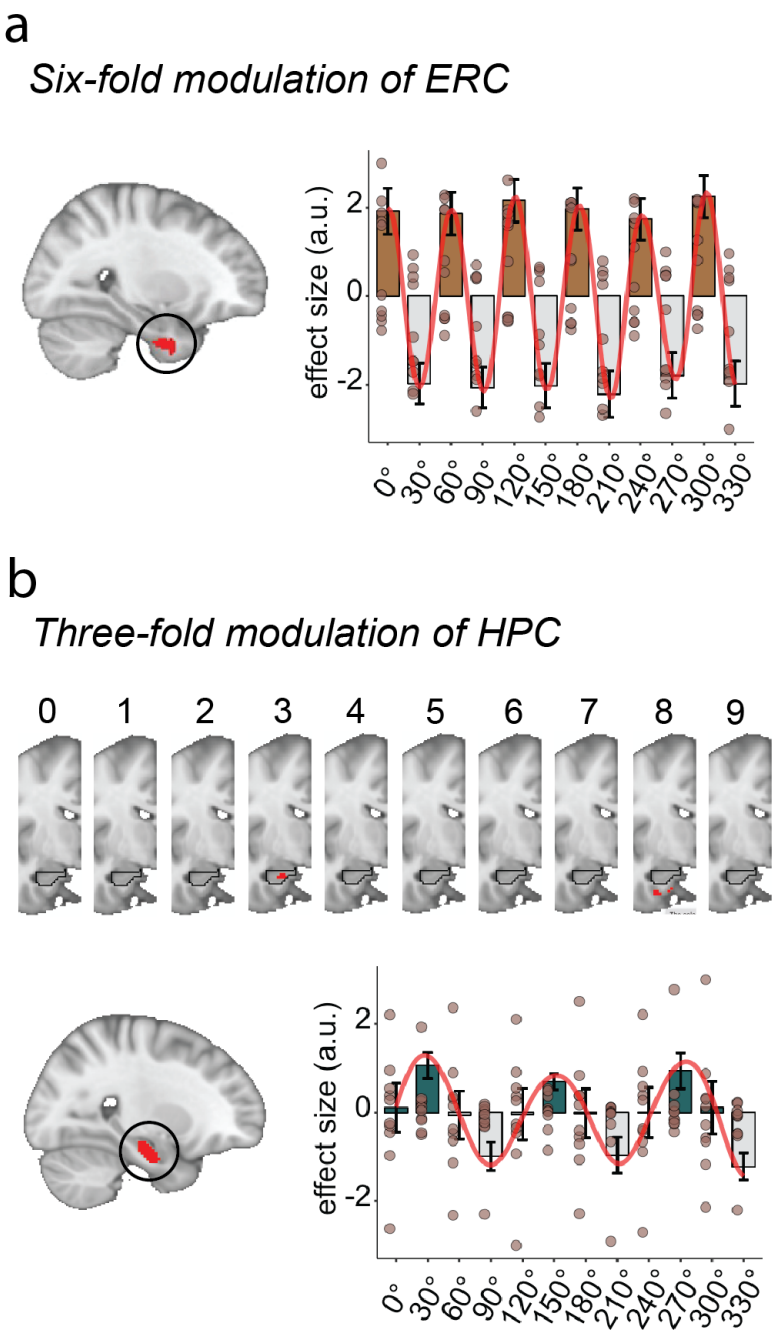

Figure S6. BOLD signal series of the ERC (black) and HPC (red & purple denoting the experimental and replication group, respectively) fluctuate as a function of movement directions (0°-360°; shown on x-axis).

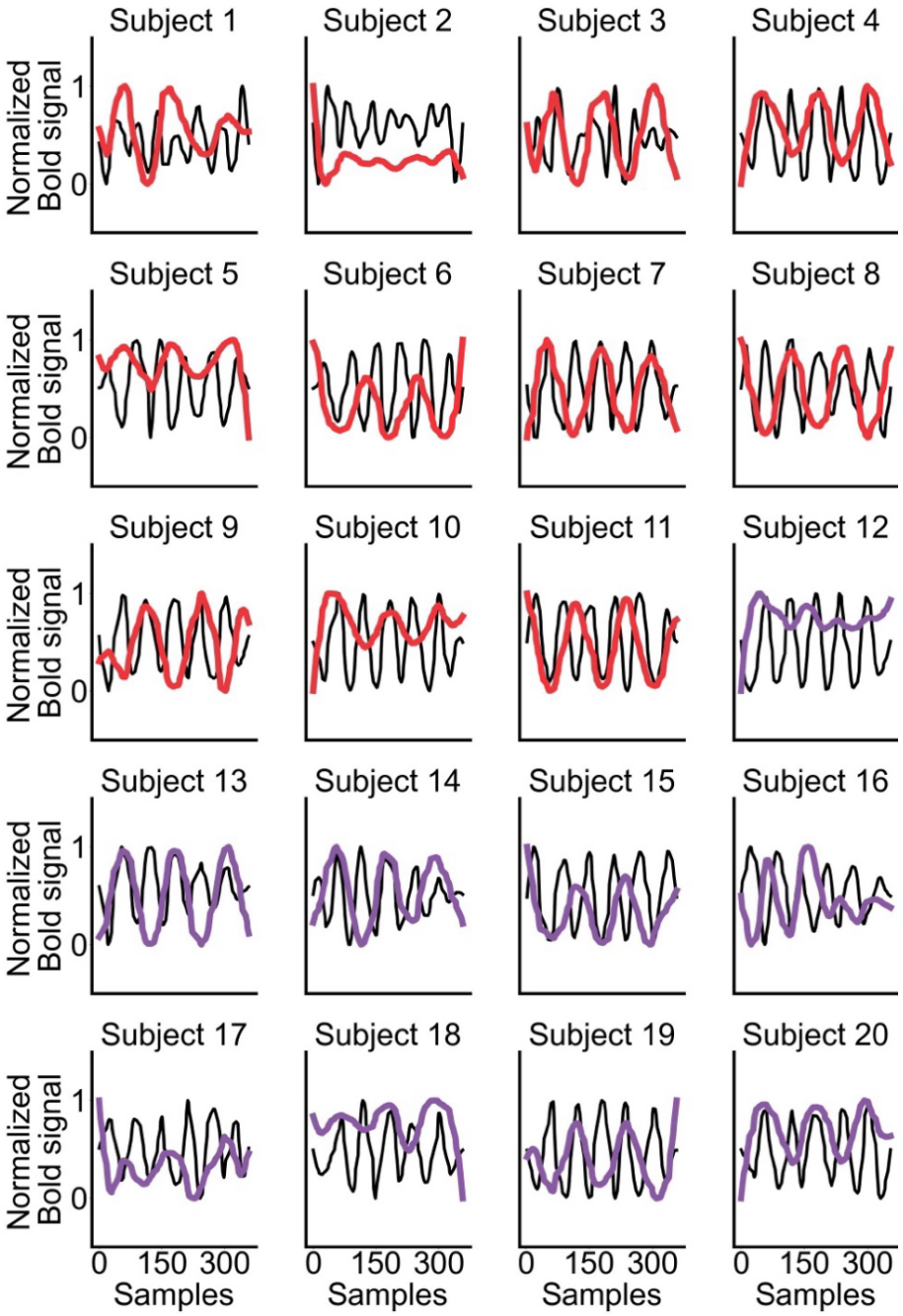
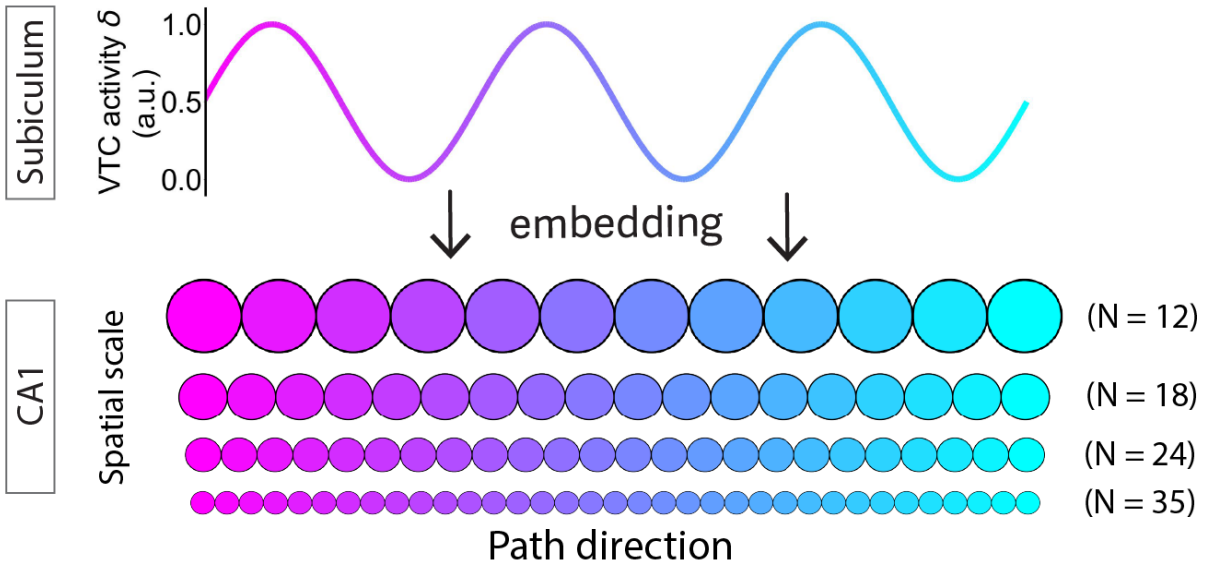
Figure S7. Schema of periodic embedding. HPC inherits the 3-fold scaffold encoded by VTC population, which embeds path directions using multi-scale encoding. In this way, coarse directions are encoded by fewer place cells, while fine-grained directions require a large number of place cells. N denotes the number of place cells.